ETH
Eidgenössische Technische Hochschule Zürich
Swiss Federal Institute of Technology Zurich

Design, assembly and measurements for a UHV chamber to be used for D^- ions trapping

Master Thesis

Matteo Simoni

July 2021

Supervisor: Dr. D. Kienzler

Department of Physics, ETH Zürich

Contents

Chapter 1

Introduction

In the following document I am going to give a description of the work I carried out for my Master Thesis in the Trapped Ion Quantum Information Group of Prof. Dr. Jonathan Home, at ETH Zürich. During the Spring Semester 2021 I was one of two Master students working on the Negative ion project, under the supervision of Dr. Daniel Kienzler and with the co-supervision of Nick Schwegler.
The Negative ion project aims at being a proof of principle of co-trapping a positive and a negative ion in a segmented Paul trap. The motivations for this project can be found both in the context of quantum metrology and of quantum computing and we will now be expanding on them.
In the next Chapters, we are going to describe the design of some of the pieces that have been inserted in the chamber, and also the assembly of the UHV chamber itself. Then, we are going to go through the many measurements done during the thesis, consisting mainly of ToF measurements and of measurements done to enhance the production rate of D^- ions.

1.0.1 Motivation from quantum metrology

An interesting application of being able to trap negative ions and in particular D^- ions, is to obtain familiarity with the trapping of $\bar{H}_2^-$, i.e. the molecular anti-hydrogen ion with same mass and charge as D^-. In our group, the molecules experiment is already obtaining familiarity with the trapping of H_2^+ with the objective of performing spectroscopy measurements. The study of the interactions between matter and their anti-matter counterpart can be extremely useful in testing the validity of the CPT theorem, a proposition of QFT that states that charge, parity and time reversal symmetry hold for every phenomenon in physics. The way in which one goes on to disproof the theorem, or to put a bound on its validity, is by very precisely measuring phenomena which would depend on differences between ratios of quantities of matter and of quantities of anti-matter. Myers pointed

out [11], that by trapping a $\bar{H}_2^-$ anti-matter molecular ion, one could perform spectroscopic measurements very sensitive to the difference between the positron-antiproton mass ratio and the electron-proton mass ratio. Also, measurements sensitive to the differences between the positron-antiproton and the electron-proton hyperfine interactions can be devised by studying $\bar{H}_2^-$. Overall, the similarity between $\bar{H}_2^-$ and D^- renders D^- a great candidate as a negative ion to be studied.

1.0.2 Motivation from the QCCD architecture

The co-trapping of a negative and a positive ion in a Paul trap can also be useful, as mentioned above, in the context of quantum computing. More precisely, the interest can be found in the development of the so called quantum charged coupled device (or QCCD) architecture for trapped ions quantum computers. The QCCD architecture is a promising candidate to develop a large scale quantum computer using trapped ions [7]. At its core, the QCCD architecture proposes to develop quantum computers as a network of ion crystals, where each ion crystal is composed by a relatively small number of ions and the connectivity between the ion crystals is obtained by moving the ions between the crystals. This scheme is in opposition to the idea of building a large scale quantum computer as a long chain of ions all in the same trap, and aims at solving considerable issues in the long chain design, namely the scalability of the optics and the large number of modes [5].
In a QCCD framework it is key to control the motion of the ions in order to implement the transport required for the coupling of different ion crystals. When using only positive ions, the axial potential in which the ions of a two ion crystal are trapped is shaped into a double well configuration to achieve said control: by moving the two minima of the double well potential, one can change the relative axial distance between the ions. This can be done by applying a given set of voltages to the various electrodes that make up the trap geometry, and by changing these voltages to shape the axial confinement as required. If instead we were using a negative and a positive ion, the axial potential of the ion crystal would need to be shaped into a third order profile, with one minimum to trap the positive ion and one maximum to trap the negative ion. As Grégoire Tomassi proved in Chapter 2 of his Master thesis [19], having to generate a lower order axial potential allows to achieve same trap frequencies and same ion distance but with considerably lower voltages on the electrodes than those required for the forth order potential needed using two positive ions. This translates into sensible advantages for the negative-positive ions configuration: achieving smaller ion-ion distances improves the coupling between the ions; also, a negative-positive ion pair would allow to obtain a larger distance to the electrode for the same ion-ion distance, thus reducing decoherence effects due to anomalous heating.

Chapter 2

Design and realization of the experimental setup

The key elements of the experimental setup are a source of negative ions and a way to co-trap them with some other positive ion. In our experiment the choice for the negative ion fell on Deuterium (D^-), while the positive ion of interest is Berillium ($^9Be^+$), as it is the lightest ion with high level control, needed to sympathetically cool the D^- ion. The setup is composed by two vacuum chambers: the first one, referred to as the D^- preparation chamber, is the one where the D^- ions are created, while the second one, referred to as the UHV chamber, is where the trap will be located. The basic idea of the experiment is to generate the D^- ions in the D^- preparation chamber, where the pressure can be maintained in the high vacuum regime, and to accelerate them and shape them into a beam that can be then directed into the UHV chamber, where the ultra high vacuum allows for trapping ions with long lifetimes. The two chambers are connected through a constriction that allows us to maintain the pressure differential. The production process involves using an electron gun (egun) to create D^- ions through dissociative electron attachment (DEA), as follows:

$$D_2 + e^- \rightarrow D + D^- \tag{2.1}$$

We will now describe in more details the various components of the experimental setup, starting with the D^- preparation chamber.

2.1 The D^- preparation chamber

Most of the D^- preparation chamber was assembled by Silvan Koch, and a more in depth study of the production of the D^- ions can be found in his Master thesis [9]. Here, we will only briefly go over the various elements of the chamber, before describing the contribution to the setup made during my time working on the project.

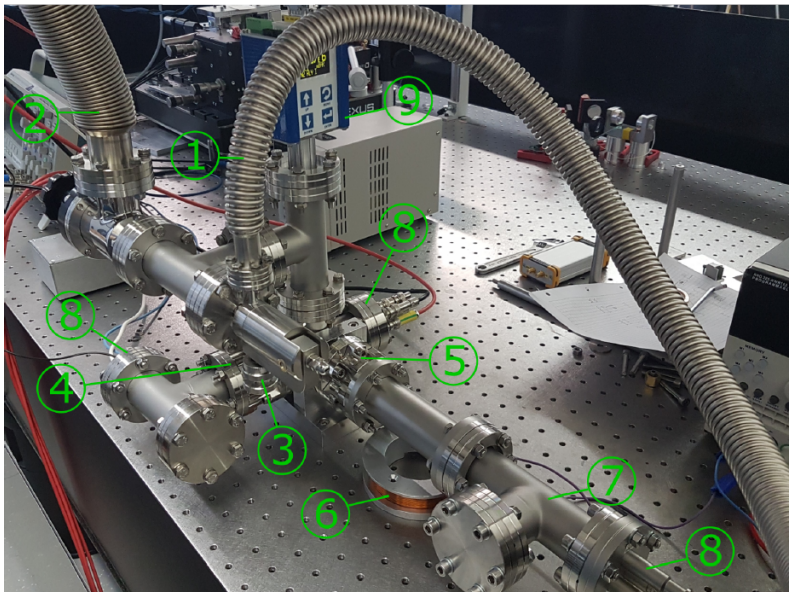

Figure 2.1: Picture of the D^- preparation chamber taken from [9]. We have: 1) tube connecting to D_2 bottle; 2) tube connecting to turbo pump; 3) leak valve to control the flow of D_2 molecules into the chamber; 4) electron gun; 5) tungsten grid to accelerate the particle and einzel lens; 6) coil; 7) microchannel plate detector (MCP); 8) some feedthroughs; 9) pressure gauge.

2.1.1 D_2 bottle and leak valve

The D^- ions are obtained from D_2 molecules thanks to the process of dissociative electron attachment; the D_2 molecules are brought into the chamber with a tube connected to a D_2 bottle. The flow rate of the molecules can be accurately controlled by turning a leak valve in the desired direction.

2.1.2 Turbo pump

The D^- preparation chamber is designed to be working at pressures in the $10^{-7} - 10^{-5}$ mbar range, so below the maximum allowed pressure for the electron gun. The pressure in the chamber is the value obtained when we have an equilibrium between sources which introduce atoms and molecules into the chamber (such as the leak valve, leakages, virtual leaks, outgassing from the walls...) and the pump, which pumps out atoms and molecules. The pump mounted to the D^- preparation chamber combines a scroll pump, which is able to pump from atmospheric pressure down to about 10^{-1} mbar and a turbo pump, which brings the pressure of the chamber down to its operating regime. The pressure in the D^- preparation chamber is measured by a Lesker ion gauge.

2.1.3 Electron gun

The electrons e^- for the DEA process of Eq. 2.1 are provided by the electron gun: a bias current I_{bias} heats up a filament which is biased at a negative voltage V_{egun}; the electrons are extracted from the filament in a controlled way with a Wehnelt voltage $V_{\text{wehn}} \lesssim V_{\text{egun}}$ applied to a shell which sits around the filament. The ratio between V_{wehn} and V_{egun} determines how much the electrons are focused into a beam, but also, together with I_{bias}, the emission current I_{emiss}, i.e. how many electrons are extracted. We usually tune the bias voltage V_{egun} around -20 V, so that the electrons have the energy at which the cross section of the dissociative electron attachment reaction we are trying to use is at a maximum.

2.1.4 Grid

In order to accelerate the D^- ions, a tungsten wire mesh, which we call grid from now on, is placed in the chamber; to the grid we apply a voltage sequence composed by a positive voltage V_{pos} followed by a negative voltage V_{neg}: the positive voltage has the function of pulling the D^- ions towards the grid, and then the negative voltage pushes them away from the center of the chamber towards the detector. The time duration of the positive pulse Δt_{pos}, the time duration of the negative pulse Δt_{neg} and the amplitudes of the two voltages V_{pos} and V_{neg} are optimized in order to maximize the count rate and at the same time in order to bunch up the D^- ions so that we can determine their mass by doing a time of flight (TOF) analysis once they reach the detector. The necessity of bunching up the D^- ions in order to do a TOF analysis stems from the fact that otherwise we would not know what kind of ions we would actually be generating, at least until after having co-trapped them with Be^+ ions. The optimization of the pos-neg pulsed sequence has mainly been carried out experimentally, both by Silvan Koch and also by me and Reza Mosala Nejad.

2.1.5 Electrostatic einzel lens

In order to focus of the D^- ions beam, an einzel lens [10] is placed in the D^- preparation chamber, after the grid. The einzel lens is constituted by a succession of three cylinders: the first and the last one are grounded, while the middle one is set at the voltage V_{lens}; the ratio between V_{lens} and the energy of the incoming beam of charged particles determines the focal length of the lens. The einzel lens also has the interesting property that it does not change the energy of a beam which traverses it in its entirety. Depending if the sign of V_{lens} is the same as the sign of the charge of the particles going through the lens or not, we can have a deceleration-acceleration einzel lens or an acceleration-deceleration einzel lens: it is worth noting that in both configurations the lens acts as a focusing element, but for a given $|V_{\text{lens}}|$

the focal length is much smaller for a lens in the deceleration-acceleration configuration; also, an einzel lens in the deceleration-acceleration configuration acts as a potential barrier for particles having an energy lower than the voltage V_{lens}.

2.1.6 Coil

The electrons which are emitted from the electron gun have the same charge sign as the D^- ions we want to produce, and thus will in principle also be accelerated and focused by the grid and by the Einzel lens; the presence of detections due to electrons on top of those from D^- ions can impede us in correctly reading the D^- ions signal that is at the basis of our experiments. With this in mind, it is important to introduce in the setup an element that allows us to deflect them away from our detector, in order to be able to work with a clean signal corresponding only to the arrival of D^- ions. In order to achieve this deflection, we place in the proximity of the chamber a coil of resistance $R = 0.08\,\Omega$ and $N = 22$ windings with its symmetry axis passing through the arm of the chamber where the grid, einzel lens and detector are located. The coil is placed about 10 cm below the center of the arm of the chamber. By applying to the coil a current of up to 11.9 A we generate a magnetic field going through the chamber and we can take advantage of the fact that the cyclotron radius for the electrons will be about a factor of $\sqrt{m_e/m_D} \simeq 60$ smaller than that for the D^- ions to deflect the electrons without affecting the trajectory of the D^- ions too much, thus obtaining a cleaner signal on the detector.

2.1.7 MCP and control system

In order to detect the presence of D^- ions in the chamber, the idea is to accelerate them into a microchannel plate detector or MCP. The MCP is an electronic amplifier device made of a wafer with millions of small channels in parallel, each of which acts as a $\times 3$ - $\times 5$ electron multiplier. The overall amplification of the signal depends on the aspect ratio of the MCP, ie on the ratio between the length of the channels and their diameter. The amplification is obtained as the charged particle, accelerated by the high voltage V_{MCP} (in our case $V_{\text{MCP}} \simeq 2700$ V) that powers the MCP, hits the walls of the channel creating an electron avalanche. When a charged particle hits it, the signal provided by the MCP at its output is a current spike whose height cannot be easily used to make deductions on the nature of the particle detected.
R. Mosala Nejad dedicated a section of his thesis to the study of the signal coming from the MCP and to the design of a control system with which to associate at every spike of the MCP a logical 5V pulse that can be more easily counted by the rest of the control system; in his thesis a lot of details

of the control system will be presented, here we just give a brief overview. The key element of the control system is that the signal from the MCP is fed to a discriminator board, which produces a square logical signal of a given length anytime the voltage from the MCP exceeds a tunable reference voltage. An efficient choice for the reference voltage is one for which minimal counts from the MCP are lost, while at the same time avoiding double counting from one of the ripples that follow a large voltage spike.

2.1.8 Deflection electrodes

As we will explain in Section 2.3, to connect the D^- preparation chamber with the UHV chamber we need a circular constriction; in order to steer the D^- ion beam into the constriction, we decided to design two couples of parallel deflection plates. The principle of operation of a couple of deflection plates is shown in Figure 2.2.

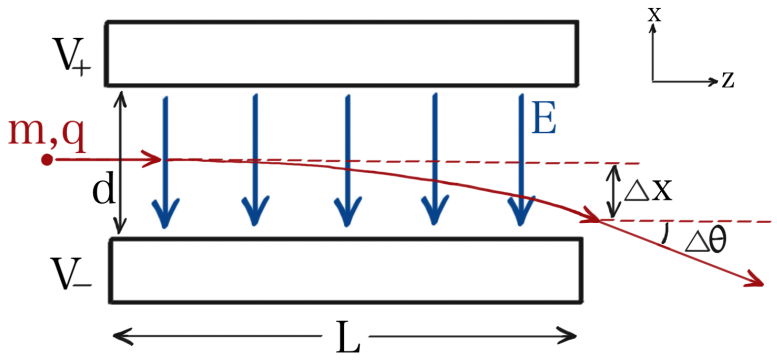

Figure 2.2: Scheme of the functioning of a pair of deflection plates. A particle of mass m and charge q gets deflected by the electric field E generated by applying voltages V_+ and V_- to the two plates of length L and distant d. The electric field offsets the particle in the x direction by Δx; when in free field, the particle will travel in a straight line with an angle $\Delta\theta$ from the z direction.

The electric field E is generated by applying different voltages V_+ and V_- to the two electrode plates respectively in order to steer the beam in a direction perpendicular to the axial direction z. In the limit of infinitely large electrode plates $L \gg d$, the electric field between the plates is constant:

$$E = \frac{V_+ - V_-}{d} = \frac{\Delta V}{d} \tag{2.2}$$

Considering a particle of mass m and charge q that has been accelerated by the negative pulse of the grid, the energy provided by the grid is much larger than the energy the particle had to begin with. Moreover, if the acceleration happens in a spatial region far away from the location of the deflection

plates, than we can assume that when the particle arrives at the deflection plates it is travelling in the z direction with constant velocity v_z given by:

$$\frac{1}{2}mv_z^2 = qV_{\text{grid}} \implies v_z = \sqrt{\frac{2qV_{\text{grid}}}{m}} \tag{2.3}$$

For our experimental setup, these are actually reasonable assumptions, as we know that the thermal energy of the D_2 molecules is about 25 meV and that the average energy transferred by the electrons to the D^- ion in the dissociative electron attachment process is about 5.1 eV, so both values are well below the energy provided by the grid. Also, simulations confirm that the acceleration of the D^- ions happens in a region around the grid much smaller than the distance between grid and deflection plates.
In the time interval L/v_z that it takes the ions to travel the length L of the deflection electrodes along z, they are displaced by the electric field of Eq. 2.2 along x by

$$\Delta x = \frac{1}{2}\frac{qE}{m}\frac{L^2}{v_z^2} = \frac{L^2}{4d}\frac{\Delta V}{V_{\text{grid}}} \tag{2.4}$$

Also, by taking the inverse tangent of the ratio between the velocities v_x and v_z at the end of the electrode section, we can compute the angle $\Delta\theta$ between the trajectory of the particle after it exits the electrodes and the z axis:

$$\Delta\theta = \arctan\left(\frac{v_x}{v_z}\right) = \arctan\left(\frac{qE}{m}\frac{L}{v_z^2}\right) = \arctan\left(\frac{L}{2d}\frac{\Delta V}{V_{\text{grid}}}\right) \tag{2.5}$$

Both the displacement Δx of Eq. 2.4 and $\Delta\theta$ of Eq. 2.5 do not depend on the charge q and on the mass m of the particle, but they only depend on a function of the dimensions of the plates ($L^2/(4d)$ and $L/(2d)$ respectively) and on the ratio between the electrode voltage and the grid voltage $\Delta V/V_{\text{grid}}$.
In our implementation we have two pairs of subsequent deflection plates, mounted such that the electric fields they produce are orthogonal to each other and so that we can obtain a deflection in both the x, z and in the y, z planes.
The electrode plate's dimensions are 7.5 mm$\times$20 mm$\times$20 mm and they are made of stainless steel. The plates are mounted with insulating rods; also, some insulating spacers divide the electrode plates, allowing us to apply different voltages on each plate through copper wires which connect them to BNC feedthroughs.
In Figure 2.3 we show the CAD drawing of the deflection plates inside the D^- preparation chamber.

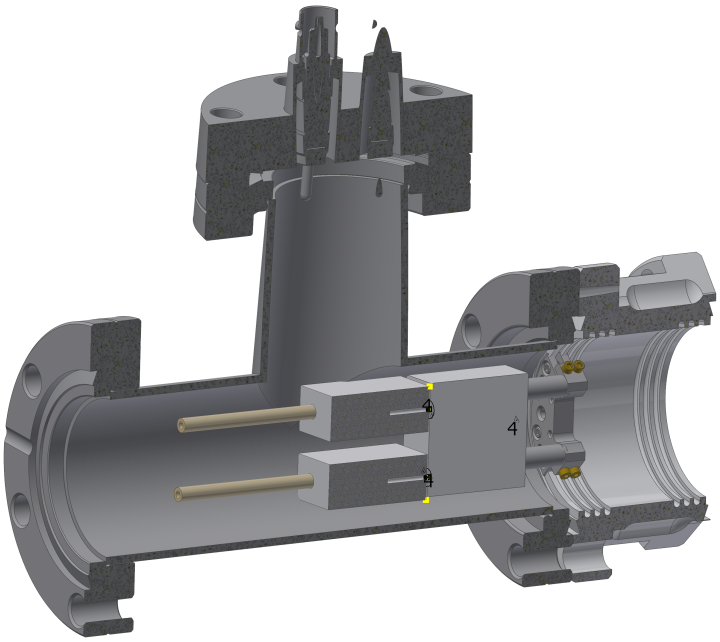

Figure 2.3: Cross section of the D^- preparation chamber showing a possible placement of the two pairs of deflection plates.

2.2 The UHV chamber

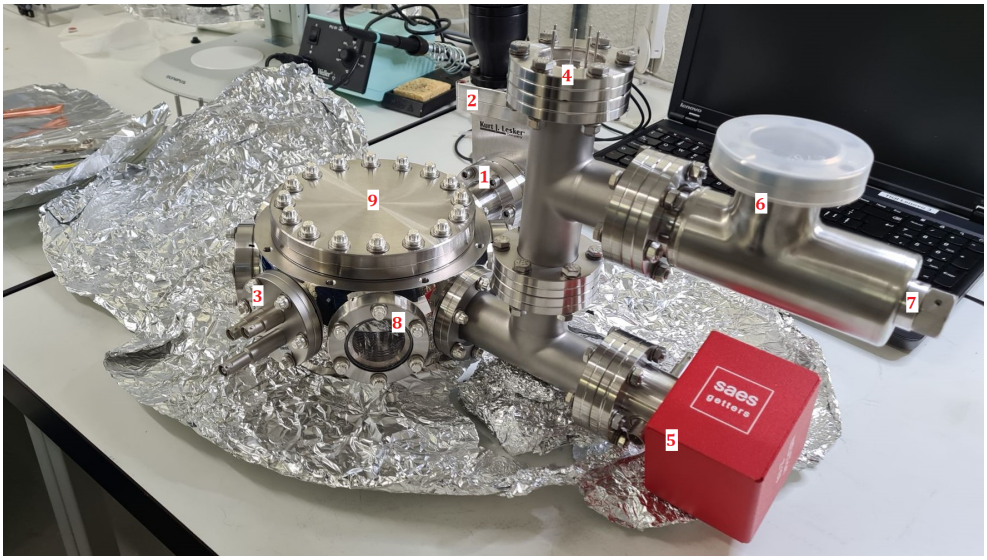

Figure 2.4: Picture of the UHV chamber. We have: 1) constriction; 2) gate valve; 3) MCP; 4) hot cathod ion gauge; 5) ion pump and getter element; 6) flange to turbo pump for the bake out; 7) valve to close off the arm to the turbo pump after the bake out; 8) side viewports; 9) blind flange.

Figure 2.4 shows the UHV chamber: it is a spherical octagon vacuum chamber with eight 2.75"CF holes on the sides and two 6.00"CF holes for the top and the bottom. On the eight side holes we connect: the constriction (1) and the gate valve (2) to the D^- preparation chamber; the MCP (3); an arm with a Lesker ion gauge (4), a NexTorr Z 100-5 SAES Getters ion pump with the getter element (5) and a flange (6) to connect the chamber to a turbopump during bake out with the relative valve to close it off (7); and five viewports (8). On the bottom we mount a large viewport and on the top a 100CF blind flange (9).
The UHV chamber is designed to operate in the regime of ultra high vacuum, which is defined as being that for which the pressure of the chamber is lower than 1×10^{-9} mbar. Usually in trapped ions experiments that do not involve cryogenic cooling, pressures of $1 \times 10^{-10} - 1 \times 10^{-11}$ mbar are obtained. In order to achieve these pressures, a series of methods and procedures have to be followed; in this section we will describe them and their implementation in our setup. In the next section we will be covering the constriction which connects the UHV chamber to the D^- preparation chamber.

2.2.1 Cleanroom procedures

To achieve ultra high vacuum, one has to minimize leakages inside the chamber, where by leakage here we mean anything that has the effect of releasing some amount of molecules and atoms in the volume of the chamber, thus increasing the pressure inside.
To begin with, there is no shortage of ways with which one could introduce contaminants inside of the chamber while in the process of assembling it. First of all, everything that goes inside of the chamber, including of course the components of the chamber themselves, has to be properly cleaned. The cleaning mainly aims at avoiding to introduce oily substances such as grease, waxes, fats and oils in general, because these tend to not be pumped out well by the pump and will keep degassing molecules into the chamber at a constant rate, thus limiting the achievable pressure. To clean all of the components going inside of the chamber, the standard procedure of the TIQI group, consisting in the following steps, has been followed:

1. Ultrasonic bath in a 5% dilution of TR3 at about 50°C for ten minutes. The TR3 is an acidic (pH = 3.0 at 1%) cleaning agent designed to remove mineral residues, flash rust, fats and oils from steel, stainless steel, ceramics, plastics and other materials [3].
2. Ultrasonic bath in a 5% dilution of RW77 at about 50°C for ten minutes. The RW77 is a basic (pH = 9.9 at 1%) cleaning agent designed to remove grease, oils, wax, resinous residues from metals, glass, ceramics, PCBs and other materials [2].
3. Rinse with tap water.

4. Blow dry with a pressured N_2 gun.
5. Ultrasonic bath in deionized (DI) water.
6. While the component is still wet, ultrasonic bath in Acetone for about ten minutes. Acetone is used as a solvent agent to remove oily and greasy contaminants from the components, but it can leave a residue when it dries.
7. While the component is still wet, ultrasonic bath in Isopropyl alcohol for about ten minutes. Isopropyl alcohol (or Isopropanol) acts as a rinsing agent for the Acetone by removing particles and evaporating without leaving residues or oily traces.
8. Blow dry with a pressured N_2 gun.

Once the components are clean, it is important to avoid contaminating them again while mounting the chamber. To minimize contamination, all the assembling has been done in a ventilated cleanroom, and by always being careful not to touch the components with tools that are not adequately clean. Wearing gloves and changing them frequently is fundamental, as introducing the fatty substances present on the human skin can lead to slow degassing oily spots that will ruin the vacuum. Protecting the component from dust particles is also relevant, but mostly when dealing with the ion trap, as specs deposited on the electrodes could cause perturbations in the electric field and have an effect on the trapping.

2.2.2 Leakages from seals and virtual leaks

One of the main sources of leakages from the outside to the inside of the chamber simply consists in molecules in the air finding their way inside of the chamber, usually through a not perfectly tight seal between different components. To minimize these kinds of leakages, we implement vacuum tight seals through CF vacuum hardware. Another concern when assembling the chamber is to prevent virtual leaks; a virtual leak happens when a small pocket of air is left inside of the chamber in a place with very small conductance to the rest of the chamber: when this happens the pocket can degas at a slow and constant rate, thus ruining the vacuum. Usually, a source of concern for virtual leaks are bolts and screws, as air can be trapped between the threads or on the bottom of the hole where the screw is tighten on. To prevent this kind of virtual leaks one can use vented screws, that have a hole in the middle to connect the bottom of the hole with the rest of the chamber.

2.2.3 Leak testing

Once the assembly is completed, it is good practice to leak test the chamber. To do that, we connected the UHV chamber to the ASM 340 by Pfeiffer Vac-

uum, a leak detector with a rotary vane pump. While spraying helium with a nozzle onto the various flanges of the chamber, we can look for spikes in the reading of the He throughput with the mass spectrometer of the leak detector: if any spikes are found, we know that some He atoms have found their way into the chamber at the flange and we can try to fix the leak. If a leak is found and isolated with this method, the first option is to try and tighten the screws of the flange in question and then to measure again the throughput of He to see if the leak has been solved. If tightening does not work, then it is necessary to open up the chamber and examine the flange with more scrutiny, to understand if maybe one of the knife edges has a dent and needs to be replaced or if other issues of this sort have occurred.
When leak testing the UHV chamber, we found a leak in the proximity of the bottom viewport. In Figure 2.5 we present a picture of the display of the mass spectrometer, showing a spike in the throughput of He atoms that goes from a baseline reading of about 1×10^{-9} mbar l s^{-1} up to about 3×10^{-8} mbar l s^{-1}. After having made sure about the location of the leak, we tried to fix it by tightening the screws around the bottom viewport: after a second leak test, the spike was no longer present, thus we conclude that the issue was solved by the tightening.
Leak testing cannot of course solve all vacuum problems, in particular a UHV can still be ruined because of contaminants on the inside, virtual leaks and degassing from the walls, and these are all issues that cannot be identified with the method we just described.

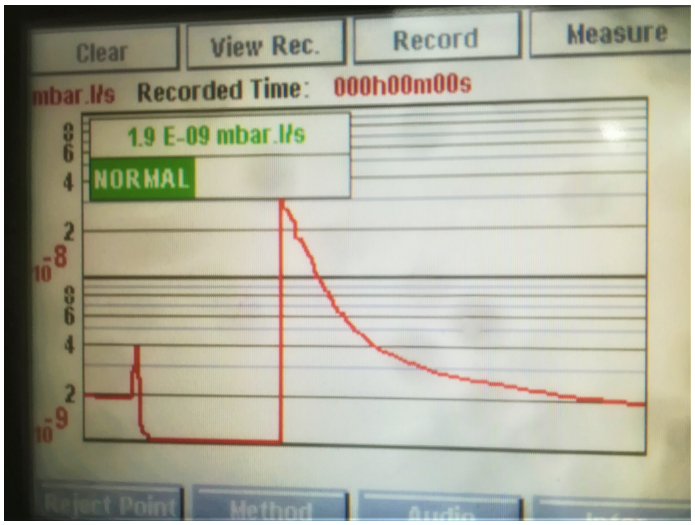

Figure 2.5: A spike in the throughput of He found when leak testing the UHV chamber

2.2.4 Bake out

In order to achieve the pressures in the UHV regime required to carry out trapped ions experiments not involving cryostats, it is necessary to minimize degassing from the walls of the chamber. Whenever the chamber is exposed to air, a certain amount of molecules, such as water molecules, are absorbed by the walls of the chamber. Once we pump down the chamber, the molecules will be outgassed from the surface at a very slow rate, thus resulting in a constant throughput that ruins the vacuum and makes it impossible to reach the UHV regime. The most common practice to solve this issue is to (soft) bake out the chamber, i.e. to heat it up to more than 100°C and to maintain the temperature for several days while pumping with a turbo pump: with the higher temperature, the outgassing rates are much higher and over the course of the several days of the bake out we deplete the amount of molecules absorbed into the walls, thus reducing the minimum obtainable pressure when we come back to ambient temperature.
When baking out the chamber, both the thermal gradient and the bake out temperature have to be monitored in order to avoid damaging any of the components of the chamber. In our case, the thermal gradient was limited by the viewports to be $< 25°\mathrm{C\,min^{-1}}$ and the temperature was limited to 200°C by the MCP mount and by the viewports. To increase the maximum bake out temperature we decided to remove the magnets from the ion pump, which would have limited the bake out temperature to 150°C; the functionality and activation of the ion pump will be described in the next subsection.
The bake out was carried out in an home made oven featuring six ceramic heaters; the heaters are turned on or off by a control system that monitors the temperature on two thermocouples that we call CONTROL1 and CONTROL2 and confronts them to the thermal gradient and to the target temperature that we set. Additionally, we also have another five thermocouples (CH1, CH2, CH3, CH6, CH7) to allow us to measure the temperature in five different spots in the chamber. We placed the two control thermocouples CONTROL1 and CONTROL2 on the two most fragile components of the chamber, i.e. the large bottom viewport and the small viewport on the left, as it was the closest one to one of the heaters. Two of the other five thermocouples were placed jointly with CONTROL1 and CONTROL2 to have a direct idea of what the control system is measuring, while the other three where measuring the temperature in the proximity of the MCP, of the ion pump and of the ion gauge. After having placed the thermocouples, the whole chamber was covered in multiple sheets of aluminum to prevent direct exposure of the chamber to the heaters; the chamber was also placed onto an elevated base to center it more inside of the oven.
While the bake out takes place, it is of course necessary for the chamber to be pumped down, so we connected it to a turbopump; the turbopump allows us to measure the pressure at its entrance, which is a decent proxy of

the pressure inside of the chamber.
In Figure 2.6 we present a report of the bake out procedure we followed by showing the temperatures measured with our thermocouples, the temperature differences again measured by the thermocouples and the pressure as indicated by the turbopump.

- The bake out started the 27th of April 2021, at about 11:00; during this first section of the bake out, which lasted until about 16:00 of the same day, we increased the temperature of the system by setting a target temperature of 100°C with a heating rate of 0.25°C min^{-1}. The heating rate that we chose is a factor of 100 smaller than the maximum thermal gradient tolerable by the viewport, but one has to take into account that the oven works by turning on and off the heaters in order to achieve the selected heating rate as an average. This means that the temperature of the chamber is subject to sharper fluctuations lasting about ten minutes as the heaters are turned on or off; when taking these fluctuations into account we found that by setting an average heating rate of 0.25°C min^{-1} we had a maximum thermal gradient of about 3°C min^{-1}, still comfortably lower than the maximum heating rate tolerable by the viewports. During the increase in the temperature, the pressure of the turbopump increased from about 8×10^{-8} mbar up to 8×10^{-6} mbar; this is of course expected as increasing the outgassing rate of water vapour from the walls is the reason for the bake out procedure.
  After the ramping up, the temperatures settled to values ranging from about 92°C for the ion pump to about 107°C for the ion gauge, and stayed there until the 28th of April at 9:00. Overnight, while the temperature was kept fixed, the pressure in the turbopump decreased from 8×10^{-6} mbar to 5×10^{-7} mbar, signalling a decrease in the outgassing rate.

- The second step of the bake out procedure took place between 9:30 and 18:30 of the 28th of April and it consisted in increasing the temperature up to about the target temperature of 147°C. The increase was done with an intermediate step, to allow for the chamber to thermalize, thus reducing the spread between the temperatures of the different components. Once again, the rise in temperature was met by an increase in the turbopump pressure, from 5×10^{-7} mbar up to 3×10^{-6} mbar. The temperature in the chamber was then kept constant until the morning of the 29th, with values ranging from 135°C for the ion pump to 156°C for the ion gauge and the pressure decreased down to 6×10^{-7} mbar.

- The third step of the bake out procedure was done between 10:00 and 19:00 of the 29th of April: we increased the temperature of the chamber

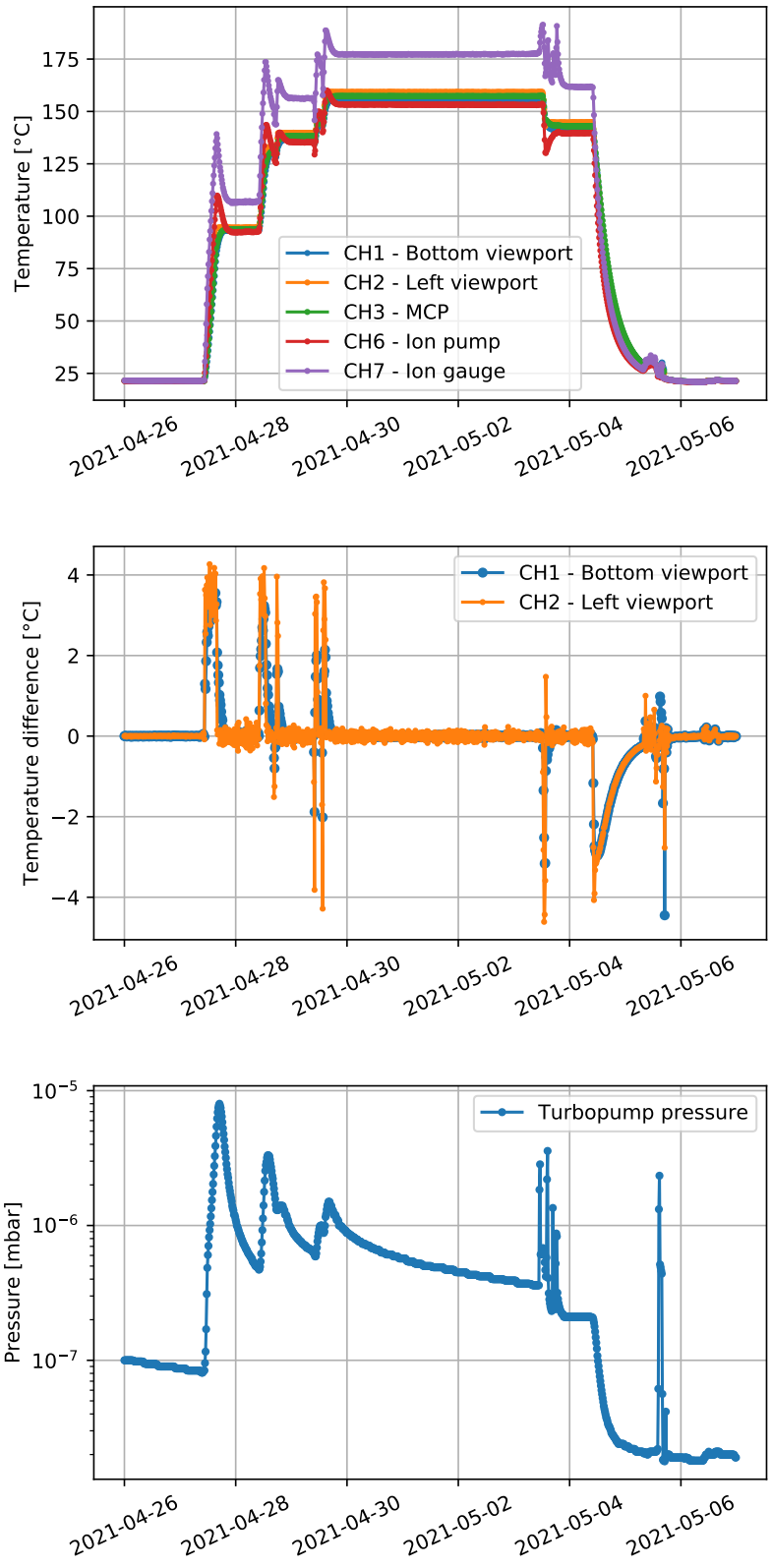

Figure 2.6: The temperatures (a) and the temperature differences (b) measured by the thermocouples and the pressure (c) measured by an ion gauge on the turbopump during the bake out

up to about the target temperature of 167°C again with an intermediary step at 157°C to allow for the thermalization of the chamber. In line with the previous steps, the turbopump pressure increased during the heating up, reaching less than 2×10^{-6} mbar. After this third and last ramping up of the temperature, we kept it constant for 90 hours, with values ranging from 153°C for the ion pump to 177°C for the ion gauge: overall, informally comparing the temperatures of our bake out with the ones achieved in other experiments of our group we were satisfied. During the days we spent holding the temperature of the chamber to these temperatures, the turbopump pressure declined down to about 4×10^{-7} mbar.

- The 3rd of May, we carried out the degassing of our ion gauge. Degassing is a procedure described in the Instruction Manual [4] of the controller of the ion gauge in use, and is needed to remove the gases absorbed into the cathode of the ion gauge. The procedure can only be followed for pressures lower than 7×10^{-5} mbar, lasts a few minutes and works by heating up the filament that is being degassed. In total we carried out six degassing, three for each of the two filaments (one lasting only two minutes and two lasting ten minutes each). Every degassing was met by an increase in the temperature of the ion gauge and by spikes in the turbopump pressure up to 5×10^{-6} mbar as the gas absorbed by the gauge was released into the chamber.
- Starting from 9:30 of the 4th of May, a complete ramping down of the temperature of the chamber was performed. The ramp down lasted until 24 hours later, when the temperature on all the CHs reached around 25°C and the pressure measured 2×10^{-8} mbar.

2.2.5 Ion pump activation

After the conclusion of the bake out procedure, while the UHV chamber is still pumped down by the turbopump, it is necessary to activate the NexTorr Z 100-5 SAES Getters ion pump that will keep pumping the chamber down to the ultra high vacuum regime. The NexTorr pump has two key elements, the first one is the NEG element, or getter, the second one is the ION element [1]. The NEG element consists in a sintered porous getter that once activated by heat reacts with active gases and sorbs them with large pumping speeds. The diode sputter ion pumping element removes methane and rare gases: electrons ionize atoms and molecules, which are then attracted to a cathode; two magnets enhance the effect by allowing the electrons to move in helical trajectories [15]. To activate the ion pump we followed these steps:

1. We opened the oven and mounted the magnets onto the back of the ION element of the pump. The magnets had been removed to allow us to reach baking temperatures in excess of 150°C.

2. We flashed the ION element: to do this, we connected the controller of the ION element to the pump and turned it on for a total of three times in a row for about two minutes each. This procedure is meant to release substances accumulated on the ION element and an increase in the turbopump pressure up to 1×10^{-5} mbar was seen as we were flashing the ION element.

3. We activated the NEG element: the getter needs to be activated by providing sufficient heat for a certain amount of time while the chamber is under vacuum; the heat is provided by a heating element inserted inside the getter. The activation procedure is needed when first using the getter or when the surface of the getter gets saturated with sorbed gases after long use, thus decreasing the pumping speed. Heating up the getter removes the layer of deposits and allows the element to work as intended. The efficiency of the activation process, that gives us an estimation of the proportion of the gases that have been removed from the surface of the getter, is:

$$\text{Activation efficiency} \propto \sqrt{D_0\, t\, \exp\left(-E/T\right)} \tag{2.6}$$

where t is the time of the activation procedure and T is the temperature of the getter during the activation. Reaching a temperature of 500°C and holding it for one hour is suggested in order to fully activate the getter. We carried out the activation by ramping the getter up to 9 V on the NEG element power supply, a process that lasted about 30 minutes. After the ramp up, we kept the 9 V on for about an hour; unfortunately our heat cable did not have a pin for temperature measurement, so we had to rely on the instructions on [1], i.e. that 9 V - 5 A for 60 minutes heat the getter up to the required 500°C. During the activation the turbopump pressure increased up to 4×10^{-6} mbar because of the gases released by the getter inside the chamber, as it can be seen with the spike in Figure 2.6 which happened the 5th of May.

After completing the activation procedure for the getter element, the turbopump pressure settled to about 1.8×10^{-8} mbar; at this point it is likely that outgassing from not baked sections of the tube going from the turbopump to the UHV chamber was the main contribution increasing the pressure, so we proceeded to isolate the UHV chamber by closing the VZCR40R angle valve dividing the chamber from the tube. The valve has to be closed with the proper torque as stress can be accumulated and relaxed during the bake out procedure. While starting to close the valve, a spike in the pressure in the UHV chamber was seen, likely due to movement and friction of the valve releasing a small amount of gases in the chamber; this did not affect the quality of the vacuum, as the gases released were pumped down in the matter of a few hours, but it broke one of the two filaments of the ion gauge.

After moving the fully isolated UHV chamber from the bake out station to its location in the lab, we let the ion pump with the getter element pump the chamber down, and in the following days the ion gauge settled to measuring a pressure of about 8×10^{-10} mbar, so a pressure in the UHV regime; also, the ion pump measurement reached its resolution limit, reading $< 2.1 \times 10^{-11}$ mbar. This discrepancy between the two readings is probably due to the fact that the measurement by the ion pump is done in the proximity of the getter element itself, so where we expect the vacuum to be the lowest.

2.3 The constriction and the pressure differential

The two vacuum chambers of our setup work in different pressure regimes. At the same time, a connection between the two is necessary in order to allow for the D^- ions to go from the preparation chamber to the UHV chamber. In order to meet both these requirements, we need to design a constriction capable of keeping the desired pressure differential between the two chambers, while at the same time allowing a passage for the D^- ions to go through. We will now describe the theory behind the design of the differential pumping constriction and show data on its functioning.

2.3.1 Vacuum theory and design of the constriction

First of all, we specify that the considerations we are going to make are valid in the context of free molecular flow, i.e. in the vacuum regime for which the mean free path of the molecules λ is much larger than D, the dimension of the vacuum vessel. In the molecular flow regime, the impacts of the particles with the walls are the predominant factor determining their trajectories, as collisions between the molecules are negligible; as a consequence, talking about the flow of the gas in a macroscopic fashion is inappropriate [20].
We define as throughput the quantity of gas crossing a plane along a duct in unit time [21]: $Q = \frac{\mathrm{d}PV}{\mathrm{d}t}$, where P is the pressure of the gas and V is the volume that flows; the throughput is measured in $\mathrm{Pa\,m^3 s^{-1}}$. We can also introduce the volumetric flow rate as the time derivative of the volume, so that $Q = P\,\dot{V}$; when talking about pumps, we define the volumetric flow at the entrance of a pump as the pumping speed S of the pump, so that the throughput of gases out of a chamber due to the pump is the product between the pressure of the gas in the chamber and the pumping speed of the pump, $Q = P\,S$.
To describe the time evolution of the pressure P in a volume V subject to pumping by a pump with pumping speed S and to a throughput Q of gas into the volume, we make use of the following continuity equation [21]:

$$V\,\mathrm{d}P = Q\,\mathrm{d}t - S\,P\,\mathrm{d}t \tag{2.7}$$

The pressure in a vacuum chamber at equilibrium can be determined by imposing that the throughput of the gases flowing into the chamber and the throughput of the gases being pumped out by the pump are equal, i.e. by setting $dP = 0$ in Eq. 2.7. One obtains:

$$P = \frac{Q}{S} \tag{2.8}$$

It is worth pointing out that generally speaking the pumping speed of the pump will be a function of the pressure, so $S = S(P)$, and also of the gas species that is being pumped.
In our systems we have two vacuum chambers, and the quantities in question will carry the subscript D^- or UHV depending on what chamber we are referring too. Starting by considering the isolated D^- preparation chamber, we can define the total throughput Q_{D^-} of gases flowing into its volume as the combination of gas flowing through leakages in the flanges of the chamber, gas outgassed by the walls and D_2 molecules being leaked through the leak valve; some of these sources can have a pressure dependence, but in first approximation we can neglect that. The pumping speed S_{D^-} of the D^- preparation chamber is the one pertaining to the turbopump connected to it; again, there will be some pressure dependence. Overall, by applying Eq. 2.8 we can determine the pressure of the isolated D^- preparation chamber:

$$P^0_{D^-} = \frac{Q_{D^-}}{S_{D^-}} \tag{2.9}$$

In an analogous fashion, we find that:

$$P^0_{UHV} = \frac{Q_{UHV}}{S_{UHV}} \tag{2.10}$$

is the pressure of the isolated UHV chamber, with Q_{UHV} corresponding to the total throughput of gases flowing into the UHV chamber and S_{UHV} being the pumping speed of the ion pump. Of course we know that thanks to the bake out procedure we drastically reduced the contribution to Q_{UHV} due to outgassing from the walls, and this is the main reason why P^0_{UHV} is order of magnitudes smaller than $P^0_{D^-}$.
We now consider a tube connecting the two chambers and ask how its presence changes Q_{D^-} and Q_{UHV}, and as a consequence P_{D^-} and P_{UHV}. In the molecular flow regime, the throughput across a tube connecting vessels 1 and 2 is proportional to the difference between the pressures in the two vessels:

$$Q = C(P_1 - P_2) \tag{2.11}$$

where C is defined to be the conductance of the tube. The throughput Q across the tube will be equal by definition to the product of $\Delta\Phi$, the difference between the impingement rates of the molecules on the two sides of the

tube, τ, the transmission probability across the tube, and $k_B T$, the average energy of the molecules [6]:

$$Q = \Delta\Phi\,\tau\,k_B T = \frac{1}{4}A\langle v\rangle(n_1 - n_2)\,\tau\,k_B T = \frac{1}{4}A\langle v\rangle\,\tau(P_1 - P_2) \tag{2.12}$$

where A is the surface are of the basis of the tube, $\langle v\rangle$ is the average velocity of a particle in the system and n_1 and n_2 are the number of molecules per unit volume in the two vessels.
Let us now consider the D^- preparation chamber and the UHV chamber to be connected by a constriction, i.e. a tube with radius R much smaller than its length L. In Figure 2.7 we show the CAD design of the differential pumping constriction that we implemented: the relevant dimension of our constriction are $R = 0.75$ mm and $L = 30.00$ mm. The piece is in stainless steel and it has been machined by the workshop of the university.

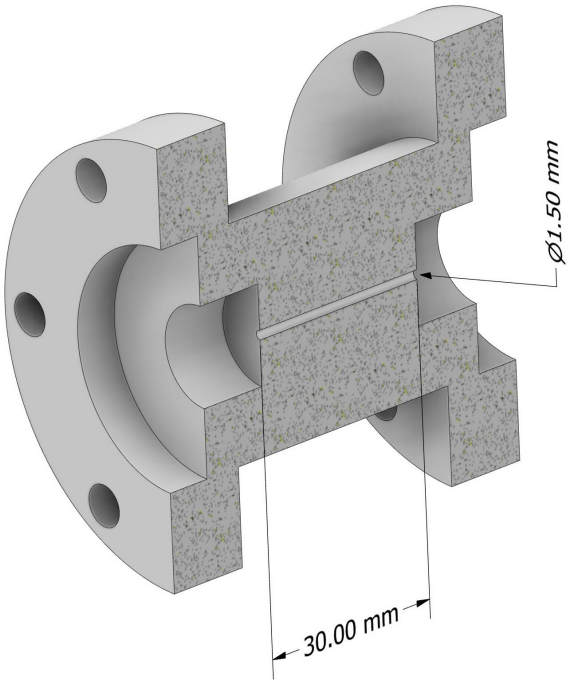

Figure 2.7: Cross section of the differential pumping constriction

Through this constriction we will have a throughput Q_C going from the D^- preparation chamber to the UHV chamber, so:

$$P_{D^-} = \frac{Q_{D^-} - Q_C}{S_{D^-}} \quad \text{and} \quad P_{UHV} = \frac{Q_{UHV} + Q_C}{S_{UHV}} \tag{2.13}$$

We want the throughput Q_C to be small enough not to destroy the ultra high vacuum we have in the UHV chamber, so it is reasonable to assume

that $P_{D^-} \simeq P^0_{D^-} \gg P_{UHV}$. With this in mind, we can expand the second term in Eq. 2.13 and obtain:

$$P_{UHV} = P^0_{UHV} + \frac{1}{4}\frac{A\langle v\rangle\,\tau}{S_{UHV}}(P_{D^-} - P_{UHV}) \simeq P^0_{UHV} + \frac{1}{4}\frac{A\langle v\rangle\,\tau}{S_{UHV}}\,P^0_{D^-} \qquad (2.14)$$

where $A = \pi R^2$, $\langle v\rangle = \sqrt{\frac{8k_BT}{\pi m_{D_2}}}$, and for a tube with $R \ll L$, $\tau = \frac{8R}{3L+8R}$ [18]. The pumping speed of our NexTorr ion pump is $S_{UHV} = 1501\,\mathrm{s}^{-1}$ for H_2, also $T = 293\,\mathrm{K}$, $m_{D_2} \simeq 4m_P$. If we insert all the numerical values of our system in Eq. 2.14 we end up with:

$$P_{UHV} = P^0_{UHV} + \left(2.4 \times 10^{-4}\right)\,P^0_{D^-} \qquad (2.15)$$

Given that the two chambers had already been designed so that when isolated $P^0_{UHV} \simeq 10^{-10}\,\mathrm{mbar} = 10^{-4} \times 10^{-6}\,\mathrm{mbar}$, with $P^0_{D^-} \simeq 10^{-6}\,\mathrm{mbar}$ for usual applications, we judge the dimensions $R = 0.75$ mm and $L = 30$ mm to be a reasonable compromise between having a constriction that does not ruin the UHV and having something that is not too difficult to machine. Also, the constriction being too tight could severely reduce the count rate of D^- ions going through it.

2.3.2 Measurement of the pressure differential

In order to test the functioning of the differential pumping constriction, after the bake out of the UHV chamber we connected it to the D^- preparation one. The connection of the two chambers was performed by closing all the way the gate valve of the UHV chamber (number 2) in Figure 2.4) and by connecting its flange to the deflection electrodes flange of the D^- preparation chamber. Then, we opened the gate valve, thus connecting the two chambers together. Apart from a temporary increase in the pressure of the UHV chamber while we were moving the gate valve, the pressures in the two chambers remained the same before and after they were connected. We then proceeded with recording the pressure in the UHV chamber after having increased the one in the D^- preparation chamber by opening the leak valve to the D_2 bottle in a controlled way. We measured the pressure in the UHV chamber both with the ion gauge and through the current to the ion pump. In total we carried out two runs, the first one while increasing the pressure in the D^- preparation chamber and the second one while decreasing it back to the starting configuration for which the leak valve was all the way closed.
In Figure 2.8 we show the results of the measurement we have just described, with the values of the pressure in the UHV chamber for the first image being measured with the ion gauge and with the values of the pressure in the UHV chamber for the second image being instead measured directly with

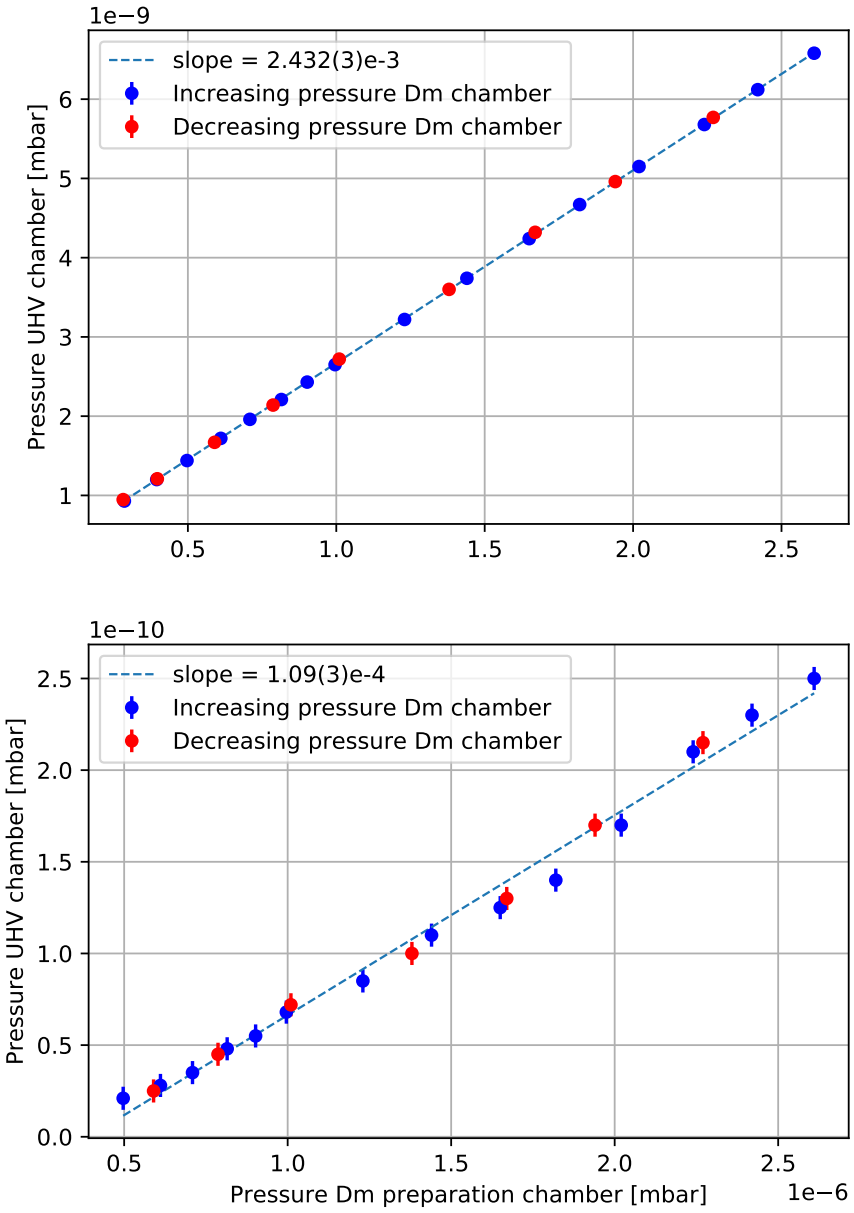

Figure 2.8: The pressure in the UHV chamber as a function of the pressure in the D^- chamber when the gate valve is left open. Pressure in the UHV chamber measured with the ion gauge (a) or with the ion pump(b)

the ion pump.
In both figures we identify with the color blue the experimental points taken while increasing the pressure of the D^- preparation chamber from a minimum of 2.86×10^{-7} mbar to a maximum of 2.61×10^{-6} mbar; in red we have the points taken while decreasing the pressure in the D^- preparation chamber back to the value of 2.82×10^{-7} mbar. For the second image we avoided plotting points for $P_{D^-} < 4.97 \times 10^{-7}$ mbar as we were limited by the resolution of the ion pump to read $< 2.1 \times 10^{-11}$ mbar.
Regarding the two linear fits, the reduced χ^2 are respectively 2.7 and 1.5. The offsets of the linear fits are not considered meaningful as in the limit of P_{D^-} tending to zero some of the approximations that we made in the previous subsection to find the linear relationship between P_{UHV} and P_{D^-} reported in Eq. 2.15 break down, for example we no longer satisfy $P_{D^-} \gg P_{UHV}$.
The two slopes are not compatible with each other: with $2.432(3) \times 10^{-3}$ the slope found for the data measured with the ion gauge is about a factor of 20 larger than the slope found for the data measured with the ion pump, equal $1.09(3) \times 10^{-4}$. The explanation for this is again probably to be found in the fact that ion gauge and ion pump are measuring pressures in two distinct places inside the UHV chamber. The slope that we find in the measurement done with the ion pump is only about a factor of 2 smaller than the one predicted theoretically in Eq. 2.15.
Overall, even though the relation between the two pressures when measured with the ion gauge is worse than expected, the differential pumping constriction proves to be working well, as it maintains a linear relation between the pressures in the two chambers in the regimes we are interested in.

Chapter 3

Measurements and data analysis

In this Chapter we are going to describe the measurements we carried out during the thesis and the data analysis that followed. Overall, we can divide the measurements in two groups, the ones taken before the assembly of the UHV chamber was completed, and the ones taken after the two chambers had been connected together. For the first ones, the data were collected with the MCP positioned in place of the gate valve that in the final setup divides the two chambers: with this configuration we did not have the differential pumping constriction, as it was being baked together with the rest of the UHV chamber; also, the deflection plates were absent. This first set of measurements was characterized by the use of a control system whose implementation with the software "ionizer" [12] that we use to control the experiment was not finalized: in particular, we were not able to record the timestamps at which the various detections happened in the detection window selected by us. Regarding the measurements taken on the final setup constituting of the two chambers being connected together, we made use of the experience accumulated with the first set of measurements to mainly analyze the time of flight of the incoming detected charged particles and to maximize the count rate of the D^- ions we are interested to trap in the future.

3.1 Measurements in the D^- preparation chamber

3.1.1 Collection of the data and basic analysis

All the measurements in the D^- preparation chamber have been taken in the following way: after having selected the experimental configuration we wanted to examine, i.e. V_{neg}, V_{lens}, V_{egun}, P_{D^-} , I_{coil}, we could still fix some parameters of the control system that determined how the measurement was performed. In general, the control system registers the counts coming from the discriminator board within a given temporal detection window;

in the version of the control system used to take measurements in the D^- preparation chamber, the detection window corresponded to the time duration of the negative grid pulse Δt_{neg}. The control system could scan the width of the detection window from a minimum value close to 0 ns up to a maximum value set by us; also, the number of different durations of the detection window that are selected in the scan was a parameter we could fix that we call the number of data points.
For every data point, i.e for every given duration of the detection window, the control system repeats the experimental sequence (positive voltage applied to the grid for Δt_{pos} and then negative voltage applied to the grid for Δt_{neg}) a number of times that we call N_{exp}, the number of experiments. While it is repeating the experiments, the control system counts the number of detections and then divides them by N_{exp} to obtain an average number of counts per experiment at that data point. After that, it moves to the next data point and repeats the procedure. Once all the data points have been scanned over, the control system starts over the whole procedure, repeating it N_{rep} times, which we call number of repetitions.
In Figure 3.1 we present an example of the type of data we collected.

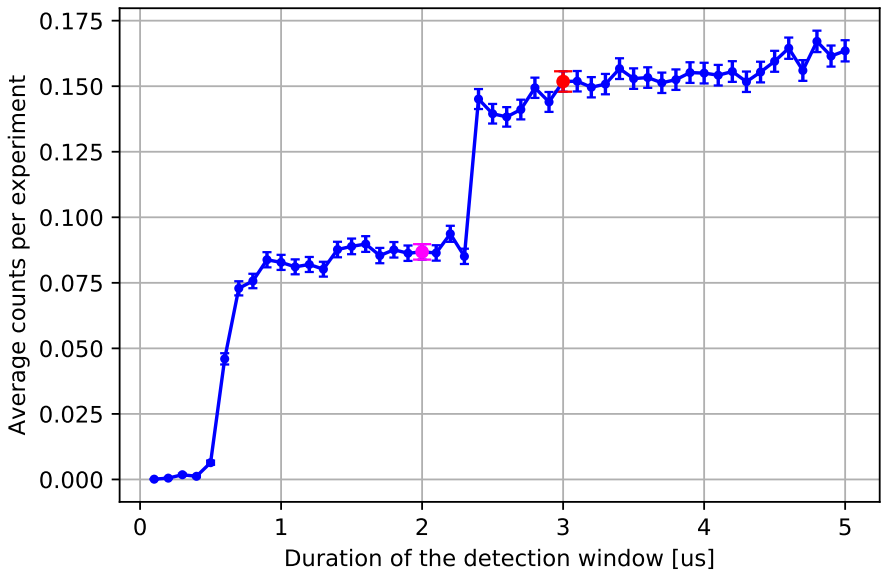

Figure 3.1: Example of the data obtained when taking a measurement in the D^- preparation chamber with the first version of the control system. The first step is due to the detection of electrons, the second one to the arrival of D^- ions. The magenta point shows that when the detection window is kept open for 2 μs, we on average measure between 0.075 and 0.100 counts per experiment, i.e. per acceleration pulse; the red point illustrates that when the detection window is kept open for 3 μs then the number of counts measured on average is about 0.150.

On the x axis we have the duration of the detection window, i.e. how many μs the detection window has been open for, and on the y axis we find the average number of detections registered by the control system while the detection window was open that amount of time. To every average number of counts $n(i)$ registered for the detection window length i we associate an uncertainty given by its shot noise:

$$\sigma\, n(i) = \sqrt{\frac{n(i)}{N_{exp} \times N_{rep}}} \tag{3.1}$$

This version of the control system does not provide any information on *when* the counts have been registered inside a given detection window, i.e it does not record the timestamps of the detections, but only determines how many counts have occurred inside the detection window on its entirety. In order to infer from this cumulative plot some information about when the counts have been measured, we can for example note that to an increase in the duration of the detection window from 2 μs to 3 μs corresponds an increase in the counts by more than 0.050, thus meaning that on average more than 0.050 detections per experiment happen in that 1 μs alone.
In Figure 3.2 we show an example of the more rigorous way we treat the bare data such as the ones in Figure 3.1 in order to extrapolate information on the time of arrival of the counts.

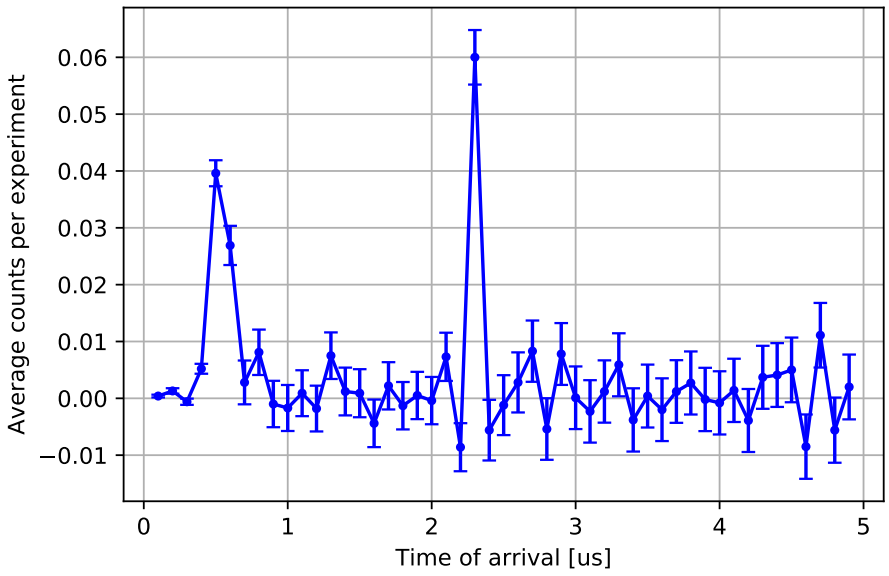

Figure 3.2: Example of the initial analysis performed on the data of Figure 3.1 in order to deduce the time of arrival of the registered counts

In a plot such as that in Figure 3.2, the value on the y axis of the i-th point is equal to the difference between the average counts registered for the i-th data point and those registered for the $i-1$-th data point of the plot in Figure 3.1. In other words, Figure 3.2 presents a sort of differential version of the cumulative data of Figure 3.1: the y value of every point i corresponds to how many more counts we measure on average by including the data point i in the detection window, i.e. how many detections happen in the data point i. The width of every data point is equivalent to the maximum width of the detection window divided by the number of data points

3.1.2 Time of Flight analysis

As we briefly mentioned beforehand, a key element of our measurements is the Time of Flight (ToF) analysis, i.e. the study of how the time of arrival of the detections depends on changes of some relevant experimental parameters; thanks to these relations we can be confident that we are actually producing and detecting D^- ions. The way in which the ToF analysis is useful in determining whether we are actually producing and detecting D^- ions is by allowing us to measure the mass (or more precisely the mass-to-charge ratio) of the detected particles; ions of different mass will have different velocities after having been accelerated by the same voltage V_{grid} and will thus reach the MCP at different times of arrival. The basic theoretical model is the following: we assume that a particle of mass m and charge q is located at the grid at time $t_0 = 0\,\mu$s with zero velocity; with the positive and negative pulse sequence, the grid accelerates the particle up to an energy qV_{grid} in a space region d much smaller than the grid - MCP distance L; the distance d corresponds to the region over which the fields from the grid decay. After travelling a distance $L - d \simeq L$ at velocity v, the particle is detected by the MCP at time $t = ToF$. During the flight, the velocity v of the ion is:

$$v = \sqrt{\frac{2\,qV_{\text{grid}}}{m}} \tag{3.2}$$

In the usual sequence of our experiment, the negative voltage V_{neg} follows the positive voltage V_{pos}, so ions located in different places or produced at different times will in general have a total final energy that is a function of V_{pos} and V_{neg}; the ideal case is for an ion to get accelerated by the positive voltage and then repelled by the negative voltage with the pull-push scheme at the basis of the functioning of the grid: in this case $eV_{\text{grid}} = q(V_{\text{pos}} - V_{\text{neg}})$ is the energy of an ion after the sequence. With Eq. 3.2 it is easy to find:

$$\text{ToF} = \frac{L}{v} = L\sqrt{\frac{m}{2\,qV_{\text{grid}}}} \tag{3.3}$$

The one in Eq. 3.3 is an ideal model that does not take into account the lens or the coil, the ramping up of the voltages on the grid, the possible

unpredicted charging up of elements of the chamber, the presence of the electrons, the initial velocity and position distributions of the ions and so on. The main predictions of this ideal model are that the ToF scales as one over the square root of V_{grid} and that from the proportionality factor b between the two we can retrieve the mass to charge ratio of the particle as:

$$b = L\sqrt{\frac{m}{2\,q}} \Longrightarrow \frac{m}{q} = 2\,\frac{b^2}{L^2} \tag{3.4}$$

In Figure 3.3 we present the result of the ToF analysis performed on the arrivals detected in the D^- preparation chamber.

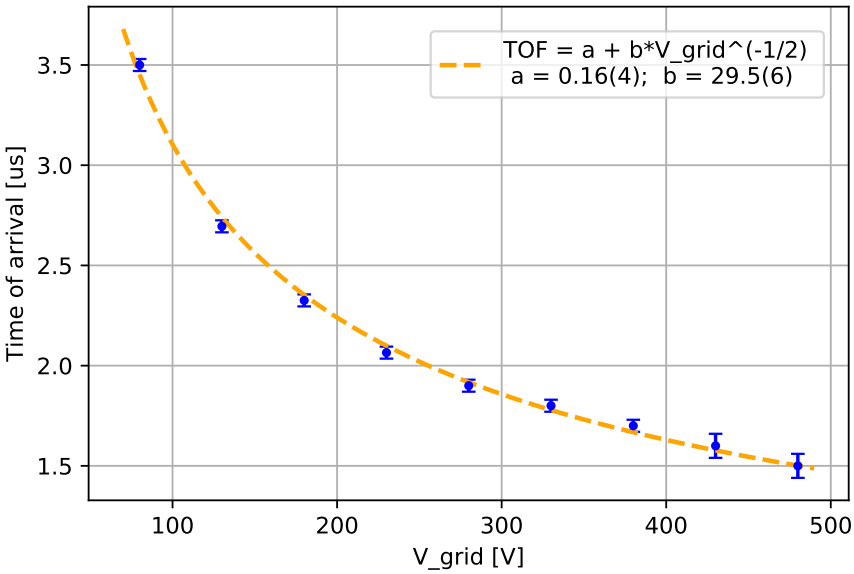

Figure 3.3: ToF analysis of the arrivals detected in the D^- preparation chamber, with fit of the ideal model of Eq. 3.3.

The ToF analysis has been done by looking at the positions of peaks equivalent to the second peak of Figure 3.2 for experiments with values of the negative voltage on the grid spanning from -60 V to -460 V. During all the measurements, we kept $V_{\text{pos}} = +60$ V, $\Delta t_{\text{pos}} = 1\,\mu$s and $\Delta t_{\text{neg}} = 5\,\mu$s, as these values were satisfactory in terms of cleanliness of the signal; in particular, we found the for longer Δt_{pos} the signal tended to appear smeared out, without clear peaks whose time of flight we could analyze. It is important to note that even though the positive voltage is set to +60 V, its ramping up time is slow and the grid only reaches +20 V, so this is the value that we added to V_{neg} in order to obtain the values V_{grid} on the x axis of Figure 3.3 for every data point. Regarding the other experimental parameters, and in

particular V_{lens} and I_{coil}, we will describe in Section 3.1.3 their effect on the detected signal in some detail, for now it suffices to say that we stuck to values that allowed us to distinguish clearly the peaks.
The reduced χ^2 of the fit of the ideal model comes out to be equal to 1.3 with 7 degrees of freedom, so we can accept the ideal model as a description of the trend of our data. From the fit we obtain an offset $T_0 = a = (160 \pm 40)$ ns not compatible with 0 ns: this is likely attributable to an offset between the instant the logical pulse to switch from the positive to the negative voltage is sent and when the actual negative voltage is applied; more on the offset of the control system can be found in R. Mosala Nejad's Master thesis.
By knowing the distance between the grid and the MCP $L = (27 \pm 1)$ cm and the parameter $b = (29.5 \pm 0.6)\,\mu\text{s}\,\text{V}^{-1/2}$ obtained from the fit, we can apply Eq. 3.4 and, by assuming that the ions have a charge $q = -e$, find the mass of the particles detected with this measurement:

$$m = (2.28 \pm 0.19)\,u \tag{3.5}$$

which is compatible with $m_{\text{D}^-} \simeq 2.01\,u$ within $1.5\,\sigma$, where u is the atomic mass unit. A slight overestimation of the deuterium ion mass is compatible with us likely overestimating of the energy of the ions, as we considered V_{grid} to be the direct sum of the positive +20 V peak reached by the grid during the positive part of the pulse sequence and of V_{neg}; this consists in the ideal case in which the ion is given the maximum energy that can actually be provided by the grid in the push-pull sequence. For a given ToF, and thus for a given velocity, if we go on to overestimate the energy of the ion it must be that we are overestimating its mass too. Overall, taking this ToF analysis into account, we can conclude that the peaks measured are indeed caused by the detections of D^- ions by the MCP.
With these considerations in mind, we can look back at the data of Figure 3.1 and understand them better: at about 2.3 μs we see a sudden increase in the average counts that we attribute to the arrival of the bunched up D^- ions. The first jump, happening before 1 μs, is thought to be due to the arrival of electrons emitted by the electron gun.

3.1.3 Effect of the Einzel lens and of the coil on the signal

In order to eventually trap the D^- ions, one needs a clean and consistent signal; for that, it is key to understand how with different experimental parameters we can isolate the ions from the electrons and also enhance their production rate. When cleaning the signal from the electrons, we can mainly try two things: changing the voltage on the Einzel lens in order to obtain a potential barrier for the electrons and increasing the current in the coil to deflect the electrons away from the MCP. In Figure 3.4 we show the results of the measurements for which we started with the standard experimental configuration described in Section 3.1.2 (also we set $V_{\text{neg}} = -260$ V) and

looked at the effect of different values both of V_{lens} and of I_{coil} on the signal.

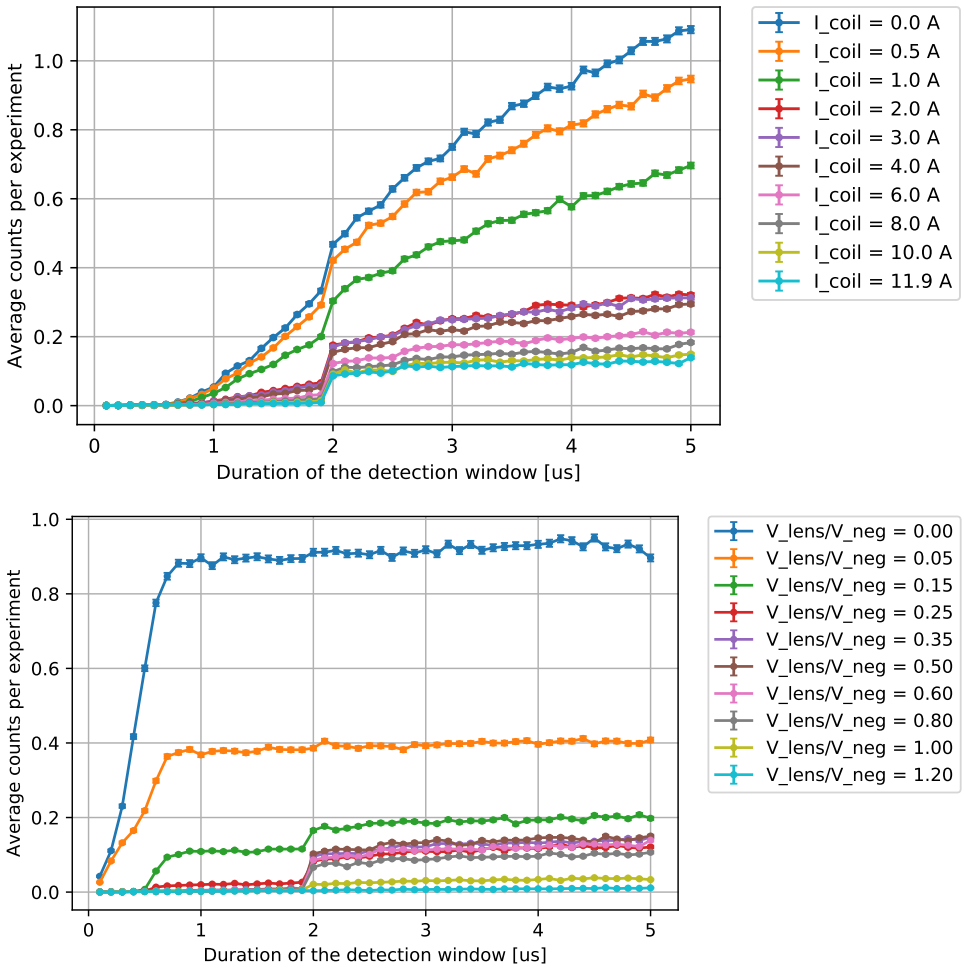

Figure 3.4: The data collected in the measurements performed in the D^- preparation chamber by changing the values of I_{coil}, in the first image, and V_{lens} in the second image. from a standard configuration

The first image of Figure 3.4 shows measurements where the value of I_{coil} was changed and where instead V_{lens} was kept fixed at $V_{\text{lens}} = 0.60\, V_{\text{neg}} = -156$ V; while in the second image, V_{lens} was varied while always maintaining $I_{\text{coil}} = 11.9$ A. These sets of measurements allow us to obtain some insight on how the Einzel lens and the coil have different effects on the signal.
By considering what happens when varying I_{coil}, we can observe that by lowering it we start to add to the sharp arrival of the D^- ions happening at about 2 μs a larger and larger constant background: for the signal being just

a line with constant positive slope, we know that the longer the detection window, the more the counts, with a direct proportionality between the two, which means that the MCP is registering counts from a constant background with no particular ToF. From this observation, we deduce that the coil is removing background counts that would otherwise be measured by the MCP, thus cleaning the signal. Regarding the source of this constant background, we cannot be certain as no time of flight analysis can be performed, which means that we have no straightforward way of knowing the mass of the detected particles. Nonetheless, it is likely they consist mainly of electrons as they are the only prevalent particle light enough to get steered by a magnetic field that does not affect the D^- ions in a relevant way. One could think the background is provided by the electrons directly shot by the electron gun itself, which provides a constant stream of electrons, but this seems unlikely because the electrons shot by the electron gun will tend to get repelled by the negative voltage that is applied on the grid for the whole duration of the detection window, especially for $V_{\text{neg}} = -260\,\text{V} \ll -20\,\text{V} = V_{\text{egun}}$; thus, we expect the vast majority of the electrons from the egun to be detected only in the short time interval while the grid is switching between the positive and negative pulses, before they get suppressed by the negative voltage on the grid. Therefore, it seems reasonable to attribute the background counts either to the few very energetic electrons from the distribution of energy of the egun that manage to bypass the negative voltage on the grid, or to those reaching the MCP via multiple walls collisions.
Let us now consider the second plot of Figure 3.4. We argue that we can distinguish two phenomena occurring simultaneously. The first one is the cleaning effect of the Einzel lens on the electron counts: by considering the measurements where we spanned V_{lens} from $0.80\,V_{\text{neg}}$ to $0.00\,V_{\text{neg}}$, we can see that the electron counts arriving at about 500 ns increase as we reduce the lens voltage. This is reasonable, as the negative voltage on the lens is acting like a potential barrier for the electrons that have an average energy of $e\,V_{\text{egun}} = 20$ eV, in a mechanism analogous to the one we proposed a few lines above to explain how the negative voltage on the grid acts as a barrier for the electrons coming from the electron gun, thus preventing us from detecting a very significant constant stream of electrons shot directly from the egun. The second effect that overlaps to the one we just described is the focusing effect of the Einzel lens: very intuitively we can see that the sharp arrival of D^- ions disappears for very large and very small ratios between the lens voltage and the negative grid voltage; this means that, as we expected, there is an ideal ratio between these two voltages for which the ions are optimally focused onto the MCP and their count rate is at a maximum. In the next section we are going to study exactly this phenomenon in more details.

3.1.4 Effect of the Einzel lens on the number of D^- ions counts

As we anticipated in the previous section, we are interested in studying the focusing properties of the Einzel lens, i.e. how for different ratios between the lens voltage and the negative grid voltage (which as we have already discussed is an approximation of the energy of the ions) we obtain different count rates for the D^- ions. To investigated this effect, we measured the number of D^- ions arrivals for different values of the ratio $V_{\text{lens}}/V_{\text{neg}}$; for the number of D^- ions counts we used the height of the peaks located in correspondence of the predicted arrival time of the ions in plots such as that in Figure 3.2. The results of the measurement are presented in Figure 3.5.

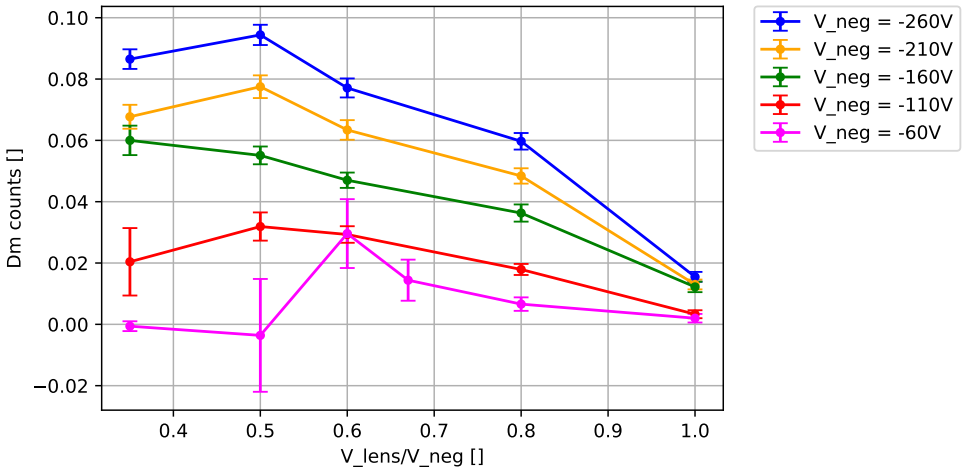

Figure 3.5: The number of D^- ions counts as a function of both the negative grid voltage V_{neg} (different colors) and of the ratio $V_{\text{lens}}/V_{\text{neg}}$ between the Einzel lens voltage and the negative grid voltage.

From the data of Figure 3.5 we can surmise a couple of considerations. First of all, we can observe how for larger (in absolute value) negative grid voltages V_{neg} we obtain more D^- ions counts; this is evident by noting that the lines for which we have more counts are the ones whose colors correspond to the lower values of V_{grid}. The dependence of the total number of counts on V_{grid} is something that we will go and study more clearly in Section 3.1.5. Regarding the Einzel lens voltage to negative grid voltage ratio, we observe that for three out of the five values of V_{neg} that we studied, the maxima for the D^- ions counts are found for the ratio being 0.5; in one case the maximum is found for ratio = 0.6 and in one case there is no clear maximum.
In Figure 3.6 we present a more complete version the measurement shown in Figure 3.5 for which we considered a wider range of ratios between the Einzel lens voltage and the negative grid voltage in the case $V_{\text{neg}} = -260$ V, spanning between 0.0 and 1.2.

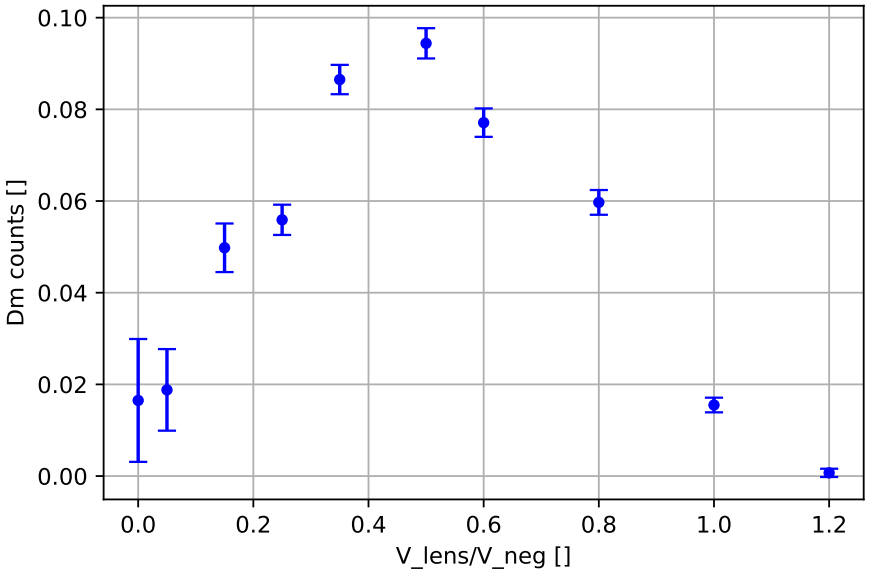

Figure 3.6: The number of D^- ions counts as a function of the ratio $V_{\text{lens}}/V_{\text{neg}}$ between the Einzel lens voltage and the negative grid voltage for the case in which $V_{\text{neg}} = -260$ V.

As expected, we observe that for values of the Einzel lens voltage larger (in absolute value) than the negative grid voltage, the lens acts as a potential barrier also for the D^- ions, thus suppressing the counts. Again, the ideal values for the ratio seem to be those between 0.4 and 0.6, with a peak at 0.5. Overall, this enhancement of the number of D^- ions counts in addition to the function as a potential barrier for the electrons coming from the electron gun that we described in Section 3.1.3, made the Einzel lens a key element of the setup in order to obtain signals clean from electrons and with decent count rates.

3.1.5 Effect of the grid voltage on the number of D^- ions counts

We have already pointed out in Section 3.1.4 that by increasing the value of V_{neg} (here still meaning by increasing its absolute value) we obtain a higher count rate. In considering how the negative grid voltage influences the number of D^- ions counts, we have to consider that having larger values of V_{neg} implies producing more energetic ions, and that more energetic ions react differently to, for example, the magnetic field B produced by the coil. In fact, the cyclotron radius R of a charged particle with velocity v in the magnetic field generated by the coil will be:

$$R \propto v\, B^{-1} \propto \sqrt{E_K}\, B^{-1} \propto \sqrt{V_{\text{neg}}}\, I_{\text{coil}}^{-1} \tag{3.6}$$

Tighter cyclotron radius have a higher probability of steering D^- ions on a trajectory not that does not intersect the MCP, thus reducing, even if slightly, the number of D^- ions arrivals. In order to prevent this effect from skewing the results of our measurement, we decided to compensate it by multiplying the value of I_{coil} it by a factor of $\sqrt{\alpha}$ for every increase by α of V_{neg}, thus keeping the cyclotron radius fixed. The cyclotron radius itself was chosen by experimentally searching for the larger value that still allowed us to detect a signal clean from the background counts. During the experiment, we were limited by the fact that the power supply we connected to the coil could not provide currents higher than 11.9 A, thus the data taken for V_{neg} being larger than about 300 V do not follow the procedure we just described and I_{coil} was kept at 11.9 A. In Figure 3.7 we show the results of the measurement.

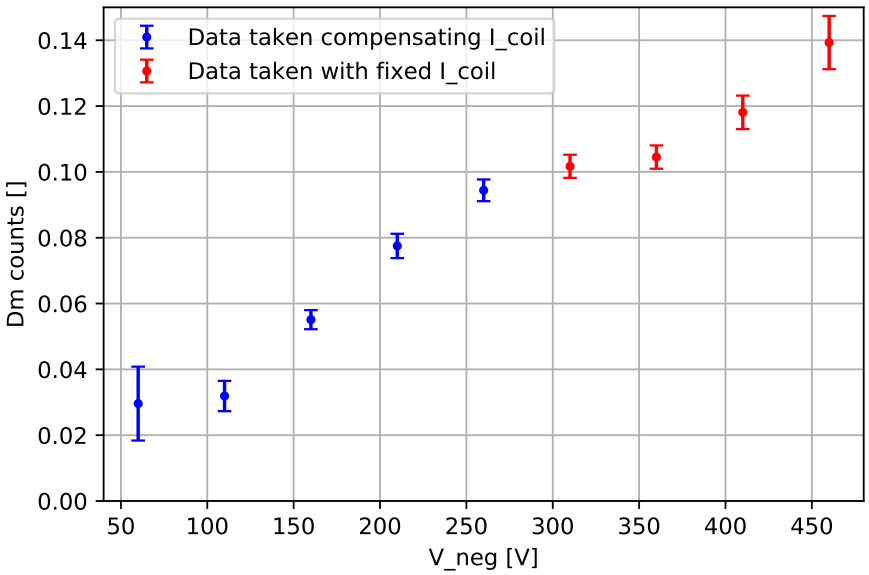

Figure 3.7: The number of D^- ions counts as a function of the negative grid voltage V_{neg}. The data in blue have been collected by changing I_{coil} to maintain the cyclotron radius fixed as V_{neg} was increased; for the data in red instead it was not possible to take them with this compensation for the reasons we explain in the text.

Even by only considering the data points in blue of Figure 3.7, which have been collected by changing I_{coil} to maintain a constant cyclotron radius, we can see a clear trend: for larger V_{neg} (again in absolute value) we measure more D^- ions counts. A possible explanation is that for larger V_{neg}, the area around the grid where ions are effected by the field and accelerated is wider, thus increasing the counts. Furthermore, more energetic ions could get less easily deflected by other fields possibly present in the chamber; plus, due to

their briefer Time of Flight they will have less time to diverge in the radial directions because of components of the momentum not oriented along the grid - MCP axes.
Regarding the last four data points in red, as we have explained we could not increase I_{coil} to keep compensating for the larger values of V_{neg}; in particular, I_{coil} should have been larger by factors of 9.1%, 17.7%, 25.6% and 33.0% with respect to the 11.9 A that we used for all the four data points. The number of D^- ions counts as we measured it still increases as a function of V_{neg}, but a broadening of the cyclotron radius will reasonably lead to an overestimation of the counts with respect to the compensated data points, so we cannot deduce the behaviour of the compensated data points as a function of V_{neg} for $V_{\text{neg}} < -300$ V.

3.1.6 Effect of the egun voltage on the number of D^- ions counts

As we briefly anticipated in Section 2.1.3, the electron gun (egun) is a key element for the production of the D^- ions. The main parameters describing the electrons emitted from the egun are their energy, how much they are focused into a beam and their number.
The electrons energy is equivalent to the negative bias with respect to ground that we apply to the egun; we call this voltage V_{egun}. The emitted electrons are focused into a beam thanks to the Wehnelt cylinder of the egun, i.e. a cap placed around and in front of the emitter of electrons apart from a small aperture; to the Wehnelt cylinder we apply a negative voltage V_{wehn} lower than V_{egun}, and the ratio between these two voltages determines how much the emitted electrons are deflected and focused. The information about the number of emitted electrons is given by the emission current, I_{emis}, i.e. the electric current flowing between the egun and ground; to increase the emission current we can act in two ways: we can either increase the bias current I_{bias} that heats up the tungsten wire from which the electrons are emitted, or we can decrease the difference between V_{egun} and V_{wehn}, as if the voltage on the Wehnelt cylinder is much lower than that on the egun the emission of the electrons will be suppressed. Within the limitations of our electron gun, we are thus able to change three experimental parameters (V_{egun}, V_{wehn} and I_{bias}) to modify the characteristics of the beam of emitted electrons, i.e. the energy of the electrons, their number and their focus.
We are now going to describe a measurement whose main purpose was to study the dependence of the number of D^- ions counts on the energy of the emitted electrons. As we have just explained, to obtain more energetic electrons it is sufficient to increase V_{egun}, but in order to maintain all the other characteristics of the electron beam fixed, we had to modify V_{wehn} and I_{bias} too. The shape of the beam, i.e. its focusing, is in principle relevant for the count rate of the ions, so we adjusted V_{wehn} together with every new V_{egun} to keep their ratio, and thus in first approximation the focus of the electron

beam, constant. Furthermore, varying the two voltages V_{egun} and V_{wehn} also modifies the value of the emission current I_{emis}, upon which in principle the number of D^- ions counts depends, so we varied the bias current I_{bias} in order to always try and keep I_{emis} fixed at 9.0 μA.
Regarding the other experimental variables not related to the egun, the data were taken by setting $V_{\text{neg}} = -260$ V, $V_{\text{lens}} = -130$ V and $I_{\text{coil}} = 11.9$ A, for the reasons discussed in the previous Sections 3.1.4 and 3.1.5.
In Figure 3.8 we present the results of the measurement described.

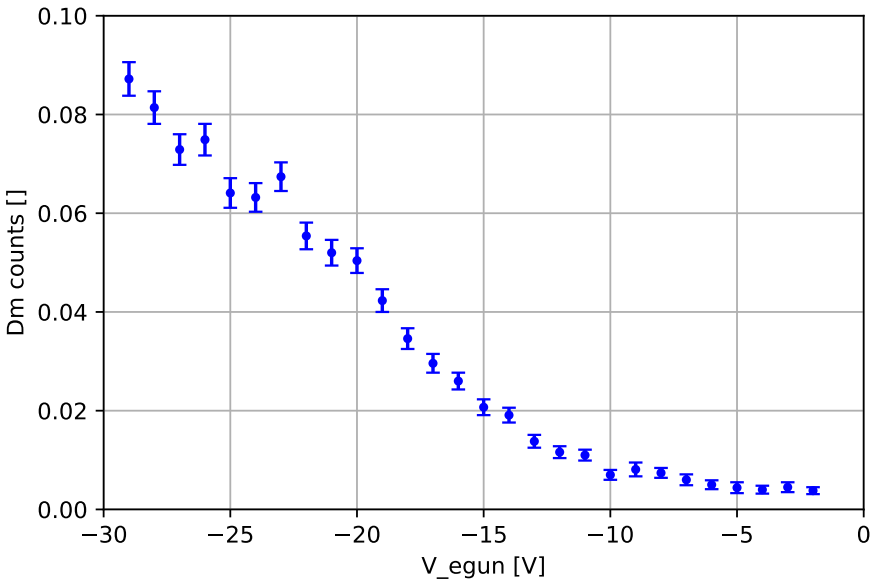

Figure 3.8: The number of D^- ions counts as a function of the voltage V_{egun} of the electron gun. The data have been collected by compensating with V_{wehn} and I_{bias} to the changes in focusing of the electron beam and in emission current that would result if we were to only modify V_{egun}.

The clear result of the measurement is that the number of D^- ions counts seem to increase monotonically as V_{egun} is lowered, i.e. as the emitted electrons are more and more energetic. We point out that the result of this measurement does not seem to be compatible with an analogous one carried out by S.Koch and presented at page 38 of his Master Thesis [9]: in his measurement, the number of D^- ions counts did not increase monotonically by lowering V_{egun}, but local maxima were found for $V_{\text{egun}} \simeq -6$ V and $V_{\text{egun}} \simeq -26$ V. The theory of the dissociative electron attachment (DEA) would predict the presence of a sharp resonance in the cross section of the process for the electrons having an energy of about 14 eV [16], which does not seem to be compatible with what was found by S.Koch and of course with the results of Figure 3.8, for which no significant peak whatsoever can

be located. This discrepancy with the theory of the DEA could be explaining by stating that the average number of D^- ions counts measured by us is not a meaningful proxy of the cross section of the reaction; this does not seem plausible though, as once the emission current and the pressure are fixed, the number of D^- ions counts is expected to only depend on the energy of the electrons through the energy dependent cross section of the reaction.
Overall, we consider this to be one of the first measurements that we performed to point away from the model of DEA as the main explanation of the production of D^- ions in the chamber. A proper theoretical background on different surface production methods can be found in R. Mosala Nejad Master Thesis, together with other measurements that provide convincing arguments going against using the model of DEA as the main explanation for the production process of D^- ions in our setup. In particular, in the context of the measurement we have just described it was impossible for us to lower the voltage of the egun further, but this constraint was lifted in successive measurements, allowing R. Mosala Nejad to probe the effect of having electrons orders of magnitude more energetic.

3.2 Measurements with the UHV chamber

We are now going to describe the series of measurements performed after the UHV chamber had been connected to the D^- preparation chamber, with the MCP located in the UHV chamber as shown in Figure 2.4. We quickly found out that the ion gauge provoked background counts on the MCP; also, we covered the viewports of the UHV chamber with aluminum foil as also photons from the outside contributed to background counts on the MCP.

3.2.1 Detection of a signal

A noticeable differences with respect to the measurements taken previously is that in order to steer the D^- ions beam into the constriction, we had now at our disposal the deflection plates electrodes. In using them, we have been grounding one of the two deflection plates for each pair of parallel plates: if we call the plates of one of the two couples L (left) and R (right) and the two plates of the other couple T (top) and B (bottom), then we grounded R and B: $V_R = 0$ V and $V_B = 0$ V. The voltages V_L and V_T have instead been provided by connecting the two plates to the output of the amplifier of the box designed by R. Mosala Nejad and described in his Master thesis. Very briefly, with a Raspberry Pi we can program a DAC to output some voltages which then get amplified by 25 times by an amplifier; the box also allows for biasing of the output signal by up to 200 V. By programming the DAC we performed a 2D scan of the voltages on the left and on the top deflection plates, producing a 2D heat map in the space of V_L and V_T.
In Figure 3.9 we present the results of two 2D scans among the many we

performed to study the arrivals on the MCP.

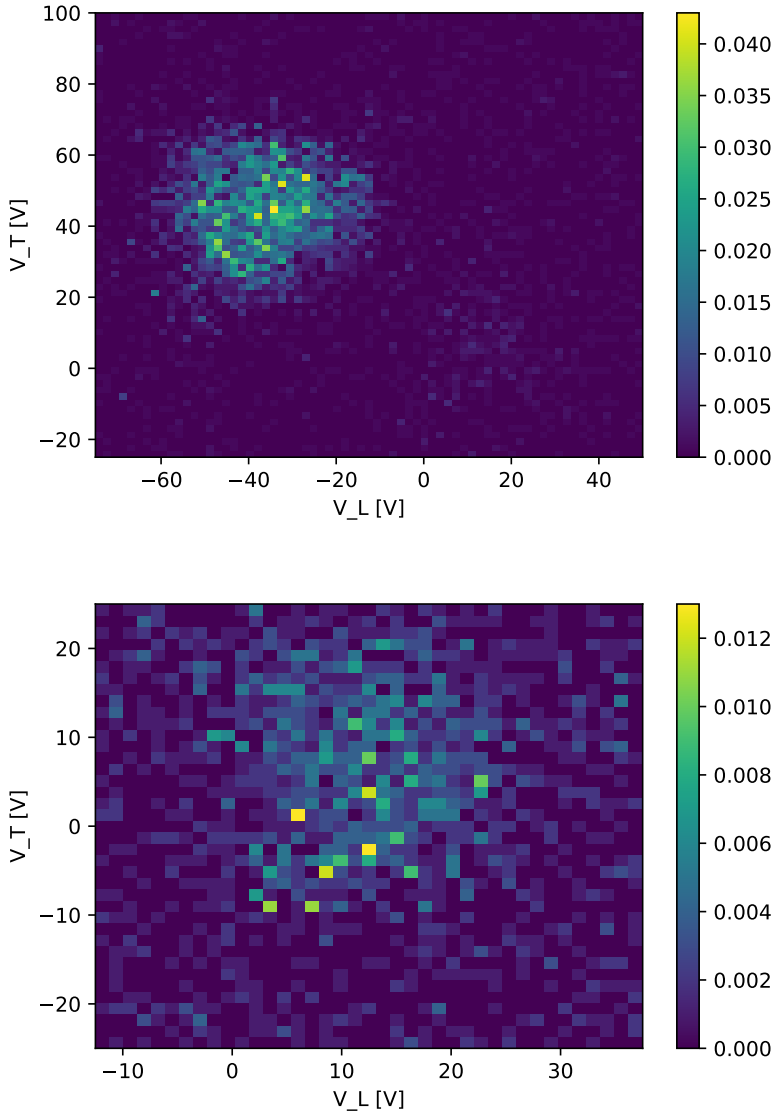

Figure 3.9: In the first image we can see the result of a 2D scan in the V_L and V_T voltage plane that covers a wide area: we observe a bright spot corresponding to the electrons counts; the arrival of D^- ions is barely noticeable. In the second image we have the result of a 2D scan focused in the area where we can see a spot corresponding to the arrival of D^- ions.

In the heat map in the first image of Figure 3.9 we can notice a bright spot around the $[-40\,\text{V}, +40\,\text{V}]$ point that we can attribute to the arrival of electrons on the MCP. Regarding the D^- ions, we can barely observe an increase in the counts with respect to the background around the $[+10\,\text{V}, 0\,\text{V}]$. In the

second image of Figure 3.9, we can more easily observe the arrival around the $[+10\,\mathrm{V}, 0\,\mathrm{V}]$ point. An evident deduction we can make from the two scans is that the electrons and the D^- ions are impacting the MCP for different values of the voltages V_L and V_T. This is compatible with the presence of a spurious magnetic field which deflects the lighter electrons: in support of this hypothesis we have the fact that by performing 2D scans while having the coil turned on, we were able to overlap the two signals for some compensating I_{coil}, as if we were cancelling an outside spurious magnetic field.
At times we have observed more than one spot pertaining to the arrival of the electrons, mostly when increasing the voltage on the electron gun. A more in depth study of the signal we get by performing ToF analysis on the arrivals of the electrons can be found in R. Mosala Nejad thesis, where the study is also related to the functioning of the control system.
Apart from the possibility of performing 2D scans, a relevant difference with respect to the measurements taken in the D^- preparation chamber is the fact that now the control system does not scan the length of the detection window, but is able to directly collect the timestamps of the counts arriving when the detection window is open.
In Figure 3.10 we show the typical result of a ToF measurement obtained with this second version of the control system.

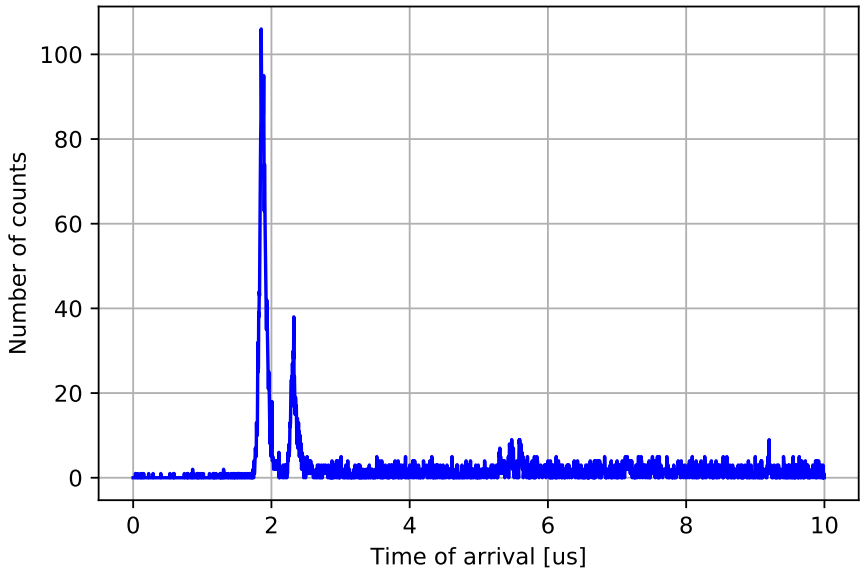

Figure 3.10: Example of a ToF measurement carried out in the UHV chamber. The control system records the timestamps of the counts arriving at the MCP and we plot the number of counts for every timestamp. In this ToF measurement we can notice the presence of two sharp peaks around $2\,\mu$s.

The first important thing that we should mention is that depending on where in the 2D space given by V_L and V_T we decide to take a ToF measurement, then the result will be different: in fact, as we have already said, the electrons and the ions pass through the constriction for different values of V_L and V_T, and a plot such as that in Figure 3.10 is retrieved only by performing a ToF measurement in the location identified in the second image of Figure 3.9. When confronting the plot of Figure 3.10 with that of Figure 3.2 that we obtained when doing ToF measurements in the D^- preparation chamber, we can notice a few differences apart from the absence of the first peak due to electrons that we have already discussed. First of all, we now observe the presence of another sharp peak about a third of the height of the first one, at about 2.2 μs; also, some arrivals seem to concentrate between 5 μs and 6 μs, even though with much less counts. All of these features of the signal, now visible thanks to the control system allowing us to take more accurate measurements, will be studied in the next sections.

3.2.2 Time of Flight analysis

A large amount of time was invested into Time of Flight (ToF) analysis of the arrivals at the MCP for the measurements performed with the UHV chamber. To begin with, we start by addressing the method that allowed us to associate to every peak in plots such as that in Figure 3.10 an actual ToF. When taking measurements in the D^- preparation chamber, we resorted to assigning to peaks such as that in Figure 3.2 a ToF given by the time of the data point for which the most counts were registered; also, the uncertainty on the ToF stemmed from the width of the data point itself.
For the measurements collected in the UHV chamber instead, the idea is to fit the counts pertaining to a given peak and obtained the ToF as one of the parameters of the fit.
When choosing the best fitting function to use, at the beginning we opted for the familiar Gaussian function:

$$G(t,\, H,\, \mathrm{ToF}_G,\, \sigma) = H \exp\left[-\frac{(t-\mathrm{ToF}_G)^2}{2\sigma^2}\right] \tag{3.7}$$

On a second look, we noticed that the arrivals present themselves as peaks with a certain amount of skewness, which cannot be captured by a Gaussian fit. Because of the skewness of the data points, the Gaussian fit ends up underestimating the number of counts for large time of arrivals and overestimating the actual ToF. In order to capture more accurately the statistical properties of the peaks corresponding to the arrivals, we opted to also fit the data points with the Doniach-Sunjic function [14]:

$$DS(t,\, H,\, \mathrm{ToF}_{DS},\, w,\, \alpha) = \frac{H\, \cos\left[\frac{\alpha\,\pi}{2} + (1-\alpha)\, \arctan\left(\frac{t-\mathrm{ToF}_{DS}}{w}\right)\right]}{(w^2 + (t-\mathrm{ToF}_{DS})^2)^{\frac{(1-\alpha)}{2}}} \tag{3.8}$$

The Doniach-Sunjic function is mainly used in solid state physics studies of metals to describe the profile of the asymmetric photoemission and X-ray lines due to Kondo interactions between the electrons of metals. Here, we adopted it seemed a good candidate in order to capture the skewness of the data. In the Doniach-Sunjic function, the parameter ToF_{DS} is approximately the position of the maximum value of the function, H is a multiplication factor, w is approximately the FWHM of the distribution and α characterizes the asymmetry.
In Figure 3.11 we present the data pertaining to one of the peaks of a ToF measurement, together with the fits performed with the two different fitting functions we have just introduced.

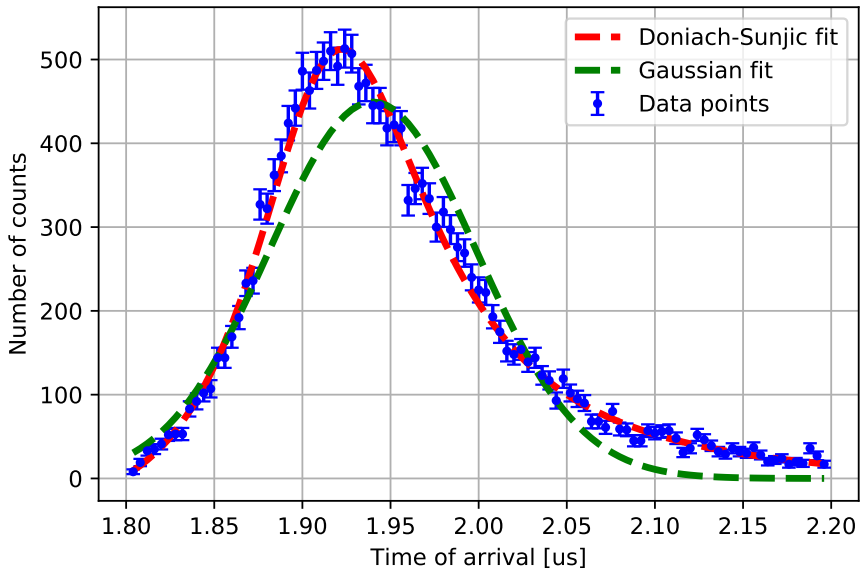

Figure 3.11: Example of the analysis of the time of the arrivals pertaining to a peak of the ToF measurement done with two different fitting function. In green we have a fit with a Gaussian distribution and in red another with the Doniach-Sunjic distribution.

To compare the goodness of the Gaussian fit with that of the Doniach-Sunjic fit, we can compute the reduced χ^2 for the data in Figure 3.11, getting:

$$\chi^2_G = 15.3 \quad \text{and} \quad \chi^2_{DS} = 1.7 \tag{3.9}$$

The results of Eq. 3.9 confirm that the Doniach-Sunjic fit is the better function to describe the trend of the data. If we look at the fitting parameters ToF_{DS} of the Doniach-Sunjic function in Eq. 3.8 and ToF_G of the Gaussian function of Eq. 3.7, we obtain the following estimates for the ToF:

$$\mathrm{ToF}_{DS} = (1.9016 \pm 0.0007)\,\mu\mathrm{s} \quad \text{and} \quad \mathrm{ToF}_G = (1.919 \pm 0.001)\,\mu\mathrm{s} \tag{3.10}$$

As we have anticipated, the two ToF are not compatible with each other. After taking everything we have discussed into account, we are going to be using ToF_{DS} as the ToF of signals detected in the UHV chamber.
To begin with, we are going to study are Time of Flight of the arrivals pertaining to the two peaks of Figure 3.10 as a function of V_{grid}, that we again define as $|V_{\text{neg}}| + 20$ V as we have discussed in Section 3.1.2. Thanks to the fact that, as we discussed in Section 3.2.1, the electron counts and the D^- counts are registered for different values of V_L and V_T, we can set $I_{\text{coil}} = 0$ A without worrying about the fact that the electrons will constitute a noisy background to the signal; also, $V_{\text{lens}} = 0$ V for this measurement. Due to the difficulty of measuring a signal for low (in absolute value) negative grid voltages V_{neg}, we scanned V_{neg} between -500 V and -1100 V. The positive voltage V_{pos} was kept fixed at +60 V; also $\Delta t_{\text{pos}} = 1\,\mu$s and $\Delta t_{\text{pos}} = 10\,\mu$s.
In Figure 3.12 we present the result of the measurement we have just described, featuring fits executed with the ideal model of Eq. 3.3 for the two peaks, that we denote as first and second peak.

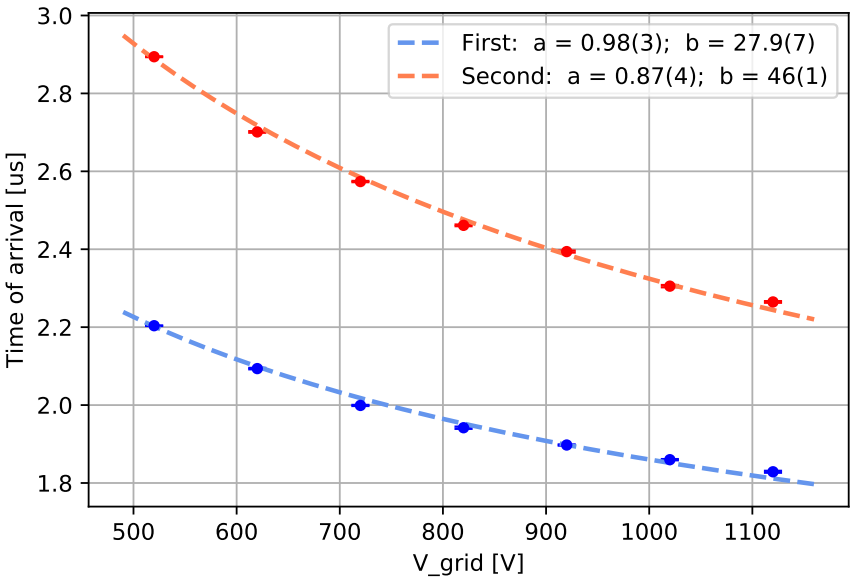

Figure 3.12: ToF analysis of the arrivals pertaining to the first peak (in blue) and to the second peak (in red) of measurements such as that in Figure 3.10, with a fit of the ideal model of Eq. 3.3.

Concerning the analysis of the first peak, the fit done with the ideal model of Eq. 3.3 is not compatible with the data points, as the reduced χ^2 is equal to 62.5 with 6 degrees of freedom; also, the residuals are not randomly distributed, which points towards a discrepancy between the ideal model and

the actual trend of the data. In the current experimental configuration, we measure the distance between the grid and the MCP to be $L = (48 \pm 1)$ cm; also, the value of the parameter b of the fit with the ideal model is $b = (27.9 \pm 0.7)\,\mu\mathrm{s\,V}^{-1/2}$; by using Eq. 3.4, we can obtain the following estimate of the mass-to-charge ratio of the particles whose counts pertained to the first peak:

$$\frac{m}{q} = (0.65 \pm 0.04)\,\frac{u}{e} \tag{3.11}$$

Neither if $q = 1\,e$, nor if $q = 2\,e$ the mass m would be compatible with an integer multiple of the atomic mass unit u. Overall, the analysis done by fitting the ideal model to the first peak of arrivals has been inconclusive in determining the actual mass of the detected particles.
We now address the analysis of the detections pertaining to the second peak. Also for this second fit we obtain a value of $\chi^2 = 63.9$, which renders it incompatible with the data points. If we neglect the incompatibility for a moment and use the parameter $b = (46 \pm 1)\,\mu\mathrm{s\,V}^{-1/2}$ we can obtain

$$\frac{m}{q} = (1.77 \pm 0.11)\,\frac{u}{e} \tag{3.12}$$

which is compatible with the mass-to-charge ratio of the D^- ions within $2.5\,\sigma$. Nonetheless, we underline once more that the fit from which we obtained the parameter b that we used to estimate the mass-to-charge ratio of Eq. 3.12 has to be rejected because of the value of its χ^2. Plus, if the arrivals of the second peak were to be due to D^- ions, we would still need to explain the nature of the first peak: the only reasonable candidate with a mass smaller than that of D^- is H^-, but the mass-to charge-ratio found in Eq. 3.11 is incompatible with $1\,u/e$. If we were to argue that the second peak is due to D^- ions counts while neglecting the incompatibility of the mass-to-charge ratio of the first peak, we would be faithfully assuming that whatever phenomenon induced the incompatibility of the first peak is suddenly no longer at play for the second peak, which would seem unlikely. Overall, more analysis have been performed to study the ToF of these peaks under different experimental conditions, and they will be covered in the next few sections.

3.2.3 Time of Flight analysis with large V_{egun}

While studying how to increase the number of counts pertaining to the first peak, R. Mosala Nejad managed to substantially boost them by a couple of orders of magnitude by increasing the energy of the incident electrons, i.e by lowering V_{egun} from the -20 V we were using so far down to -400 V. A description of this remarkable measurement will be detailed in his Master thesis. From the point of view of the investigation of the production mechanism of D^- ions, this measurement can be seen as a major extension of the one described in Section 3.1.6, in which we observed a trend apparently in

contradiction with what we would be expecting from the theory of the DEA. In R. Mosala Nejad's measurement, V_{egun} could be set to values lower than before thanks to the evolution of the control system of the experiment.
The measurement we have just briefly described was very important in allowing us to achieve more counts in less time, thus boosting the signal to noise ratio that we could obtain for a measurement of a given length; thanks to this improvement, we could take other ToF measurements that allowed us to discern more clearly some of the features of our signals.
In Figure 3.13 we present the result of a measurement with $V_{\text{egun}} = -200$ V.

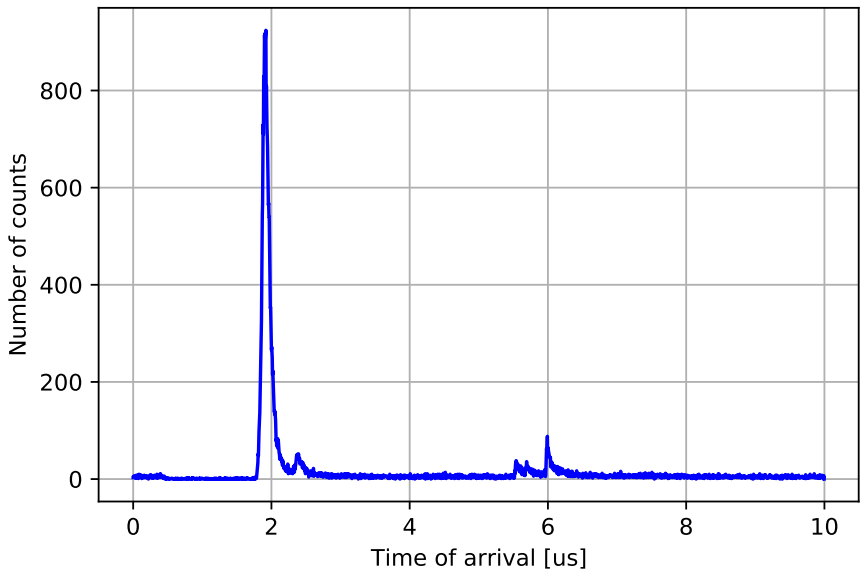

Figure 3.13: Example of a ToF measurement carried out in the UHV chamber by setting $V_{\text{egun}} = -200$ V. We can notice the presence of the first sharp peak around $1.9\,\mu$s, the second one around $2.3\,\mu$s and a third one around $3.0\,\mu$s; also, another couple of smaller peaks can be seen between $5.5\,\mu$s and $6.0\,\mu$s

When confronting the results of Figure 3.13 with those of Figure 3.10, we can notice first of all that the height of the first peak is almost an order of magnitude larger. Also, apart from the first two peaks, we can more clearly distinguish a third peak at $6.0\,\mu$s and two smaller ones just before.
From now on, we will keep referring to the peak that in Figure 3.13 is located just before $2.0\,\mu$s as the first peak and to the one at about $2.5\,\mu$s as the second peak; plus, the peak at exactly $6.0\,\mu$s will be called the third peak. The smaller peaks located between $5.0\,\mu$s and $6.0\,\mu$s were to noisy to be meaningfully studied, so we avoided doing that.

Overall, we carried out two runs of measurements of the ToF as a function of V_{grid}, for $V_{\text{egun}} = -200$ V. In Figure 3.14 we present the results of the ToF measurements for the three main peaks for the two runs.

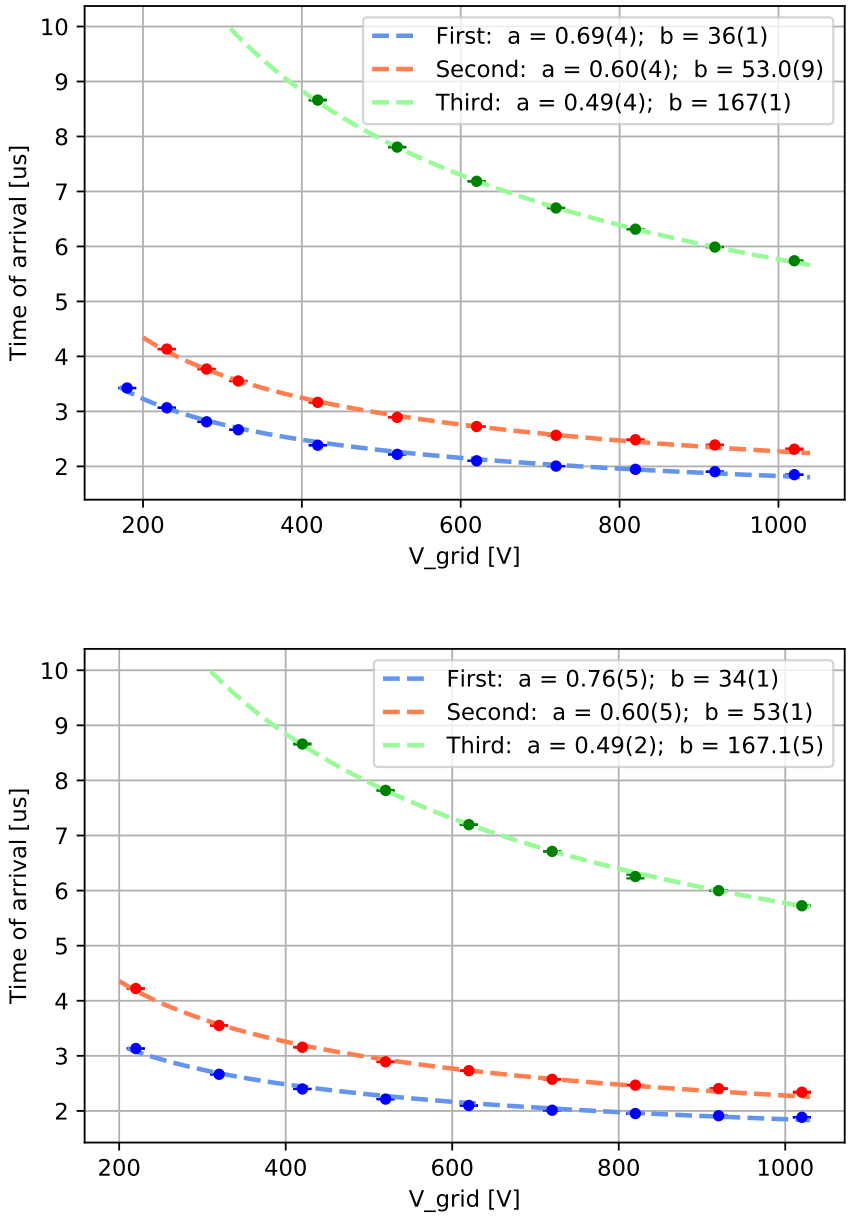

Figure 3.14: ToF analysis of the arrivals pertaining to the first (in blue), second (in red) and third (in green) peaks of Figure 3.13, with a fit of the ideal model of Eq.3.3. In the first image we have the results of the first run, in the second image we have the results of the second run.

In order to characterize the measurements shown in Figure 3.14, we present the key results in the following Table.

Peak	Run	χ^2	$a\,[\mu s]$	$b\,[\mu s\,V^{-1/2}]$	$\frac{m}{q}\,[\frac{u}{e}]$
First	1	1019.9	0.69 ± 0.04	36 ± 1	1.07 ± 0.07
First	2	787.0	0.76 ± 0.05	34 ± 1	0.99 ± 0.08
Second	1	63.9	0.60 ± 0.04	53.0 ± 0.9	2.33 ± 0.13
Second	2	67.1	0.60 ± 0.05	53 ± 1	2.35 ± 0.13
Third	1	13.5	0.49 ± 0.04	167 ± 1	23 ± 1
Third	2	2.9	0.49 ± 0.02	167.1 ± 0.5	23 ± 1

Table 3.1: Table showing the main results of the fits shown in Figure 3.14.

The first thing that we observe is that the reduced χ^2 obtained by fitting the ideal model are not acceptable, especially for the measurements pertaining the first two peaks. It is possible that by using the uncertainty on the fitting parameter ToF_{DS} of the Doniach-Sunjic function of Eq. 3.8 we are systematically underestimating the uncertainty of the ToF of the peaks, but nonetheless it does seem that the second and especially the third peak agree with the ideal model of Eq. 3.3 more than the first peak, which may be indicative of some mass dependent effect that modifies the distribution of the arrivals from the ideal case.
Secondly, we notice that for every peak the parameters a and b and also the mass-to-charge ratio m/q are always compatible between the two different runs; this is evidence of the repeatably of the experiment. Nonetheless, the parameters and the mass-to-charge ratio found in this measurement pertaining to the first two peaks are not compatible with the ones found in the measurement described in Section 3.2.2 when setting $V_{egun} = -20$ V: in principle of course this is not to be expected as we changed the experimental configuration by increasing the voltage of the electron gun, still this would imply that the energy of the incident electrons has some effect on the ToF of the particles in the chamber.
Another observation can be done with respect to the various offsets a that we obtain from the fits: even though the offsets of measurements of the same peak in different runs are always compatible with each other, the offsets relative to the first and to the third peaks are not. If the offset were to only be due to a delay of the control system, then there would be no reason to expect it to depend on the mass of the detected particle.
Lastly, let us consider the mass-to-charge ratios. From the measurement, we obtain that the mass-to-charge ratio of the first peak is compatible within 1 σ with 1, which strongly points towards the fact that we are detecting H^- ions. Regarding the second peak, we find that the detections are compatible

within 2.5 σ with something having a mass-to-charge ratio of 2, which could be indicative of D^- or of H_2^-. For the third peak, the mass-to-charge ratio lies between 21 and 25 (95% confidence interval).
Neither the mass-to-charge ratio found for the first peak nor that for the second peak are compatible with the ones obtained from the measurement described in Section 3.2.2 when $V_{\text{egun}} = -20$ V, suggesting a non trivial dependence of the ToF dynamics on the energy of the incident electrons, something that the ideal model of Eq. 3.3 that we are using for the fitting does not capture.

3.2.4 Time of Flight analysis with large I_{emis}

After taking the measurements described in Section 3.2.3, other experiments were run in the setup and the shape of the signal changed over the days. In Figure 3.15 we show the signal observed in a measurement performed three weeks after the one reported in Figure 3.13.

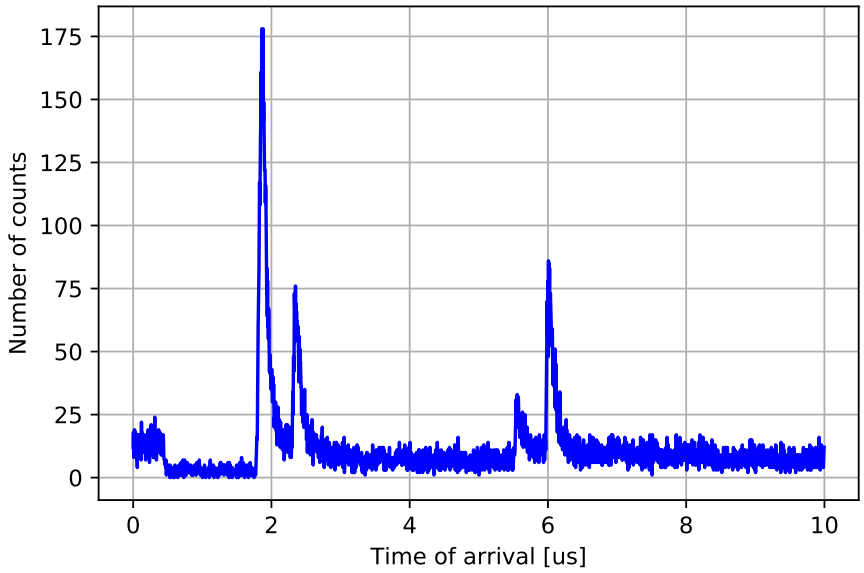

Figure 3.15: Example of a ToF measurement carried out in the UHV chamber by setting $V_{\text{egun}} = -200$ V. We can notice the presence of the first sharp peak around 1.9 μs, the second one around 2.3 μs and a third one around 3.0 μs; also, another couple of smaller peaks can be seen between 5.5 μs and 6.0 μs

It can be seen that, on top of the first, second and third peak observed previously in Figure 3.13, another peak, that we will refer to as "new", is now present before the usual third peak at 6 μs. Moreover, the relative height

of the peaks varied, with the height of the first peak in particular that decreased with respect to the others.
In Figure 3.16 we present a ToF measurement performed for the first, second, third and new peak shown in Figure 3.15 for which we increased the value of the emission current of the egun, from $I_{\text{emis}} = 30\,\mu\text{A}$ to $I_{\text{emis}} = 120\,\mu\text{A}$, in order to understand if the presence of a larger number of electrons floating in the chamber would be affecting the ToF.

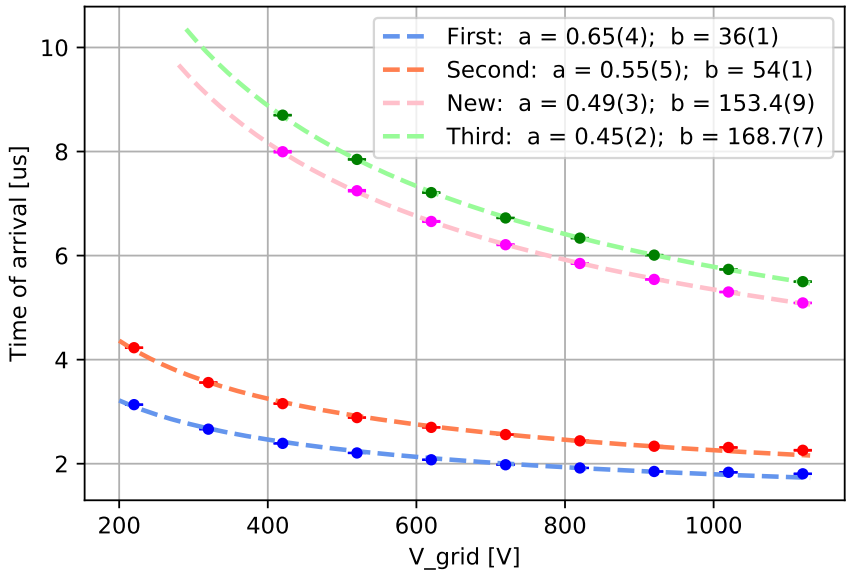

Figure 3.16: ToF analysis of the arrivals pertaining to the first peak (in blue), to the second peak (in red), to the third peak (in green) and to the new peak (in magenta) like those in Figure 3.15, with a fit of the ideal model of Eq. 3.3.

To characterize the measurements of Figure 3.16 we collect all the key results in the following Table.

Peak	χ^2	$a\,[\mu\text{s}]$	$b\,[\mu\text{s}\,\text{V}^{-1/2}]$	$\frac{m}{q}\,[\frac{u}{e}]$
First	536.6	0.65 ± 0.04	36 ± 1	1.10 ± 0.07
Second	166.3	0.55 ± 0.05	54 ± 1	2.41 ± 0.13
Third	10.3	0.45 ± 0.02	168.7 ± 0.7	24 ± 1
New	3.1	0.49 ± 0.03	153.4 ± 0.9	19.6 ± 0.8

Table 3.2: Table showing the main results of the fits shown in Figure 3.14.

The reduced χ^2 of the first, second and third peak are too large and ren-

der the fit statistically incompatible with the data point; the trend of the χ^2 is the same as the one observed for the measurement with $I_{\text{emis}} = 30\,\mu\text{A}$, i.e. it is larger for the measurement of the first peak and smaller for that of the third and new peak. When analysing the parameters of the fits of the measurement, we find a complete agreement with those obtained in the measurement described in Section 3.2.3, where we studied the ToF for the voltage of the egun still at -200 V and the emission current at $30\,\mu$A. In particular, the values of the offsets a and of the parameters b of the fit for the first, second and third peak are compatible with the one obtained previously. Also, the mass-to-charge ratios for each run are compatible with the mass-to-charge ratios of the previous measurement.
When studying the mass-to-charge ratio of each peak, we notice that the one for the first peak is compatible with 1, which, as we have explained, corresponds to H^-. For the second peak instead, the mass to charge ratio is compatible with 2, i.e. with that of D^- and of H_2^-, only within $3.2\,\sigma$. Still, it is not compatible with any other mass to charge ratio apart from 2.5, which anyway would not indicate any reasonable molecular or atomic ion.
If we now consider the new peak, the offset $a = (0.49 \pm 0.03)\,\mu$s is compatible with both the offsets of the second and of the third peak. Regarding the mass-to-charge ratio, it lays between 18 and 21 (95% confidence interval). In [13] we find as potential candidates the molecular anions DO^- and H_3O^-, which have a mass-to-charge ratios of 18 and of 19 respectively.
Overall, when considering the results of the measurement described in this section with that of Section 3.2.3 where the emission current was four times lower, the results strengthen the evidence that the first peak is due to detections of H^- ions and that the second peak is due to detections of D^- ions or of H_2^- ions.
Lastly, we point out that setting the egun to larger values of the emission current did not result in statistically significant changes in any of the values obtained from the fits.

3.2.5 Charging up hypothesis

When trying to extrapolate information about the nature of the detections from ToF measurements, we started questioning whether some elements of the chamber left erroneously floating could charge up and affect the ToF of the particles. The proposed mechanism is that the electrons emitted from the egun that strike the floating element of the chamber will charge it up until the charged up element will produce a potential landscape stopping the electrons from continuing to arrive. Such a phenomenon would leave an element in the preparation chamber charged up to a voltage V_{charge}, which could in principle affect the trajectories of the particles and their ToF; the ideal model does not take charging up into account and this could induce mistakes in the attribution of the masses of the particles.

To test whether this charging up could be affecting the ToF of particles in the chamber, the following measurement was devised. We disconnected the first cylinder of the Einzel lens from the terminator connector that usually grounds it to the outside of the vacuum chamber and we connected a capacitor with capacitance C = 7 nF between the cylinder and ground. By doing so, the cylinder was floating, with a total capacitance to ground of $C + C_{\text{lens}}$, where $C_{\text{lens}} = 20$ pF is the capacitance of the cylinder to ground without adding the capacitor C in parallel. By leaving the electron gun running within the experimental sequence, the cylinder and the capacitor C will charge up to the voltage V_{charge}. We have then measured the voltage V_{charge} by connecting the oscilloscope through a $\times 10$ attenuation probe to the cylinder and capacitor C: this discharged the pair over the $10 \times 1\,\text{M}\Omega$ of the oscilloscope and allowed us to measure V_{charge} and the characteristic time of the discharge that is expected to be $\tau = 10 \times 1\,\text{M}\Omega \times 7\text{nF} = 70$ ms.
In Figure 3.17 we present the scheme of the circuit we have just described that we used for the measurement.

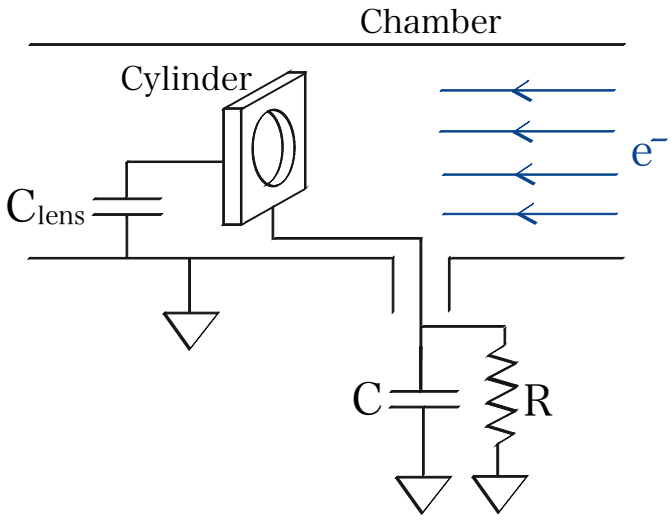

Figure 3.17: The circuit that we have employed to study the charging up of a floating element in the chamber. The cylinder of the Einzel lens has a capacitance C_{lens} to ground, $R = 1\,\text{M}\Omega$ is the resistance of the oscilloscope and C is the capacitance of the capacitor we placed in parallel to the cylinder.

As soon as we connected the oscilloscope to the floating cylinder, the discharge could be visualized on the oscilloscope as a negative spike in voltage followed by a relaxation over the characteristic time τ.
In Figure 3.18 we present a screenshot showing the results of a measurement for which the voltage on the electron gun was set at V_{egun} = -20 V.

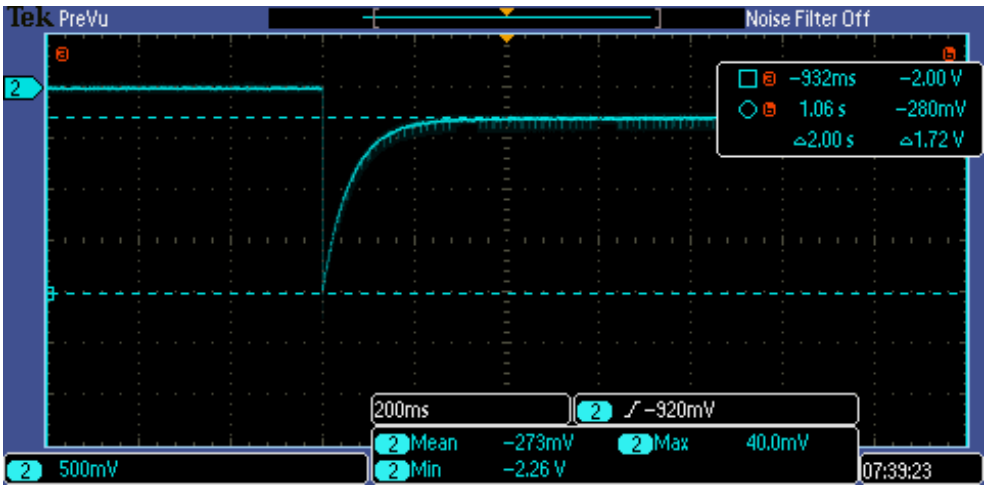

Figure 3.18: Screenshot of the oscilloscope for a measurement done with V_{egun} = -20 V. The oscilloscope is connected at the beginning of the fourth division, in correspondence to the negative voltage spike.

From the measurement of Figure 3.18 we can observe that the negative voltage on the cylinder drops by 17.2 V after connecting the oscilloscope. After turning off the egun, another 2.4 V drop are observed: this means that the electrons from the egun charge the floating lens cylinder down to V_{charge} = -19.6 V. The characteristic time can be computed by considering a voltage drop of $1/e$ and comes out to be 68 ms, where the expected one is 70 ns.
From a similar measurement performed after setting the electron gun to V_{egun} = -10 V, we obtain that V_{charge} = -9.4 V. We consider these results as evidence supporting the fact that a floating element in the chamber charges down to about V_{egun}. This is reasonable, as once $V_{\text{charge}} = V_{\text{egun}}$ electrons from the egun will be repelled by the charged element and an equilibrium voltage is reached.
By taking two ToF measurements, the first one after having charged up the cylinder down to $V_{\text{charge}} \simeq -20$ V and the second one after having grounded the cylinder, the ToF for the first peak for V_{neg} = - 1000V were measured to be $(1.838 \pm 0.004)\,\mu$s and $(1.833 \pm 0.012)\,\mu$s respectively. This testifies that, at least for $|V_{\text{egun}}| \ll |V_{\text{neg}}|$, the eventual charging up of an element of the chamber will not affect the ToF of the particles significantly.
Overall, these measurements of the charging of one of the cylinders of the Einzel lens allowed us to determine the likelihood of some elements of the chambers charging down to V_{charge} if left floating. Moreover we now have more elements with which we could characterize the effect of this charging on the ToF of the particles in the chamber, if we wanted to elaborate a model more complex than the ideal one.

3.2.6 Drift of the total number of counts

As we have anticipated in Section 3.2.4, the shape of the signal has been changing with time ever since the voltage of the egun V_{egun} was brought to -200 V. This change has mostly consisted in the height of the first peak pretty constantly decreasing with the days as we were taking more and more measurements and the other peaks either remaining constant, or decreasing slightly or even increasing slightly. Overall then, the relative height of the peaks was changing over the days and we had no predictive power to understand the future evolution of the signal from the chamber.
The proposed mechanism at the origin of the drift in the number of counts is the following: the very energetic electrons strike the tungsten grid and this releases H^- and D^- ions absorbed into it. It is reasonable to expect that if the process we are probing is particularly efficient, then by leaving the egun running for long periods of time we end up depleting the reservoir of particles in the grid, thus lowering the overall count rate. With this mechanism in mind, we would expect the grid to replenish once the egun is turned off as this would allow for the molecules in the chamber to be absorbed. This proposed mechanism goes hand in hand with the production of the ions being understood as a surface process in which the energetic electrons aid the desorption of the ions from the metal by exchanging momentum [8], and would not be compatible with DEA being the predominant process as in that case no drifts in the number of ions is expected to happen due to P_{D^-} and I_{emis} being kept constant.
In order to test these ideas we performed a measurement of the drift of the total number of counts pertaining to the first peak (that we tend to attribute to H^- ions) and to the second peak (that we tend to attribute to D^- ions). The drifting has been measured over days and alternating periods over which the egun was left running at $V_{\text{egun}} = -200$ V to other periods during which it was turned off, to observe if there was some replenishing of the number of counts. The emission current I_{emis} and the other experimental parameters were kept fixed to avoid attributing the drift to changes of other parameters. The measurement can be seen as serving three objectives:

1. In order to eventually trap the D^- ions, it is useful to understand how to achieve repeatability for the signal that we generate in the D^- preparation chamber. This repeatability strongly depends on us understanding if and how variables such as V_{egun} affect not only the production rate itself but also the overall availability of molecules in the tungsten grid over time.

2. Correlating a drift in the number of counts with having energetic electrons shot at the grid while the pressure is kept constant can serve as strong evidence that the dominating production channel does not consist in DEA, but in a surface process for which the ions are desorbed

from the metal.

3. Measuring the evolution of the number of counts pertaining to the first and to the second peak under changing experimental conditions can help us identify the nature of the particles whose detections pertain to the first or to the second peak.

In Figure 3.19 we show the result of the measurement we have just described.

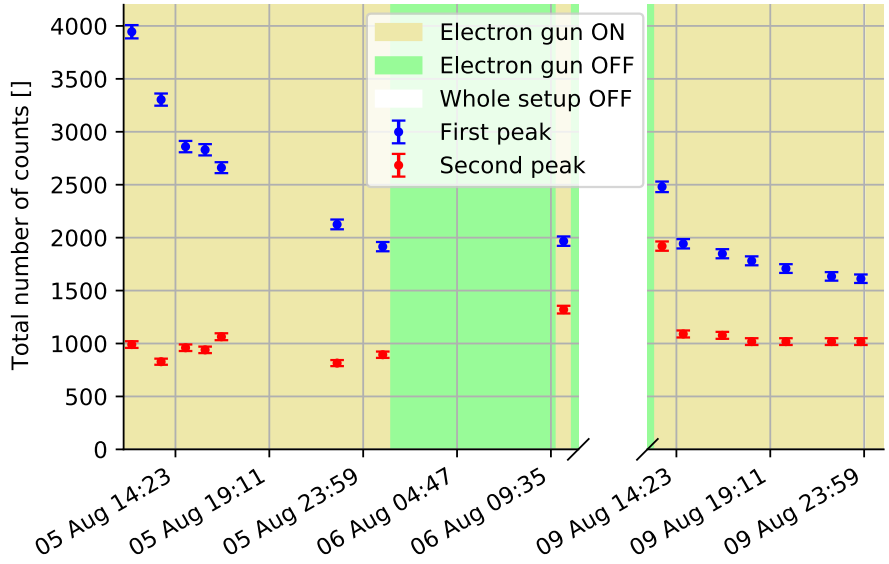

Figure 3.19: Measurement of the drift of the total number of counts pertaining to the first (in blue) or to the second (in red) peak. In yellow we indicate the time interval for which the egun was left running with $V_{\text{egun}} = -200$ V, while in green we have the regions for which the egun emission current was totally suppressed. In white we indicate a three days period over which the whole setup, including the egun, had been turned off.

By observing the data in Figure 3.19 we can notice right away the drift in the number of counts pertaining to the first peak in the intervals during which the egun is left on at $V_{\text{egun}} = -200$ V: during the first 11 hours of the measurement, the total number of counts from the first peak dropped by 50%, from being a factor of 4 larger than those from the second peak to being 2 times larger. The counts pertaining to the second peak held stable for the whole duration of the first section of the measurement.
After having left the egun off for about 8 hours, the counts from the first peak did not change, while those from the second peak increased by about 50%. We then waited three full days with the setup turned off with the goal of understanding if it was possible for the counts from the first peak to

recover back to the starting value. After three days we can see an increase in the number of counts from both peaks, but already after a couple of hours of the egun being on, both drop to lower values, with the counts from the first peak still dropping below the values from three days earlier and the counts from the second peak holding stable at the usual level.
By the end of the measurement, the counts from the first peak have dropped by 60% with respect to the initial value (from 4000 to 1600), while the ones from the second peak have have not changed significantly.
We interpret the results of this measurement as being compatible with the first peak being due to detections of H^- ions and the second one being due to detections of D^- ions. In fact, it is possible that decreasing V_{egun} by about one order of magnitude to -200 V allowed us to extract a substantial amount of H^- ions from the tungsten grid, but the fact that the vast majority of the particles in the chamber are D_2 molecules made it impossible for the H reservoir in the grid to be replenished. This could be the reason why we have observed a constant decrease in the number of counts pertaining to the first peak, while the ones from the second peak have been stable: D_2 molecules floating in the chamber can constantly replenish the losses due to the D^- ions being produced, thus an equilibrium is reached.

3.2.7 Time of Flight analysis with H_2

In order to clear any residual doubts on the nature of the particles detected, we opted to exchange the D_2 bottle for a H_2 bottle and to fill the chamber up with H_2: looking at the shape of the signal and at the ToF of the particles in the chamber would have been helpful to distinguish the nature of the particles pertaining to the various peaks. The D^- preparation chamber was filled up with H_2 closing the gate valve from the UHV chamber, turning off the turbo pump and isolating the scroll pump; then, the D^- preparation chamber was filled up to 0.9 bar with H_2 and left for four full days.
The main idea of the experiment is that during the venting, the tungsten grid would be filled with H_2 molecules from the chamber. This could have a few consequences on the shape of the signal. If no difference whatsoever were to be registered from the shape of the signal for example of Figure 3.15, then the likely explanation would have been a profound lack of understanding on our part about the nature of the production process, as filling out the chamber with H_2 molecules would not have resulted in the expected changes. If another peak were to appear for mass-to-charge ratio smaller than that of the "first peak", then it would have been reasonable to attribute this one to H^- ions and to rethink the applicability of our ideal model to predict the mass of the particles pertaining to a given peak. The expected outcome was an increase in the number of counts from the first peak, that previous analysis suggested should be attributed to H^- ions, likely accompanied by a decrease in the number of counts from the second peak.

In Figure 3.20 we present the signal we obtained after carrying out a ToF measurement in the experimental conditions we have just described.

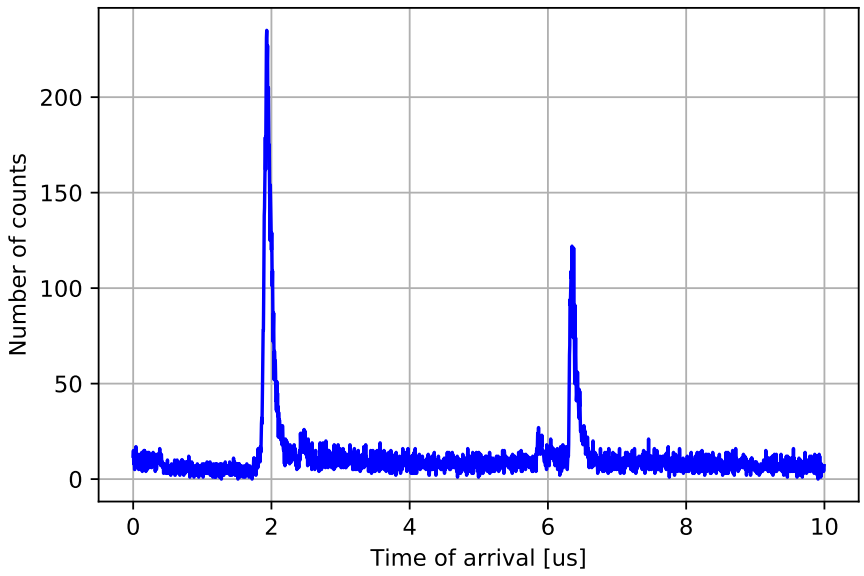

Figure 3.20: Example of a ToF measurement carried out in the UHV chamber after having vented the D^- preparation chamber with H_2 molecules for four days. We notice that the second and the new peaks from Figure 3.15 are now barely noticeable; also the number of counts pertaining to the first and to the third peak are now larger.

The clear difference between the result we have got in Figure 3.20 and the shape of the signal reported in Figure 3.13 and in Figure 3.15 is the very low number of arrivals pertaining to the second peak, which was not distinguishable enough from the background counts for us to perform any ToF measurement on it.
Apart from the fact that the D^- preparation chamber had been filled up with H_2 molecules for a few days, there are no other differences with respect to previous measurements to be noted, concerning both the experimental sequence or other experimental parameters, thus we can attribute the difference in the shape of the signal to the venting of the chamber.
Interestingly, also the new peak disappeared and this could be a clue in trying to understand what's the nature of the arrivals, as we would expect that a decrease in the number of D_2 molecules in the chamber would also contribute to having less counts of any molecular ion composed by D ions. In particular, already in Section 3.2.4 we had discussed how the mass of the particles of the new peak were compatible within $2\,\sigma$ with $18\,u$, the mass of the anion DO^-.

In Figure 3.21 we show the ToF measurement done for the first and the third peak present in Figure 3.20, by varying V_{neg}.

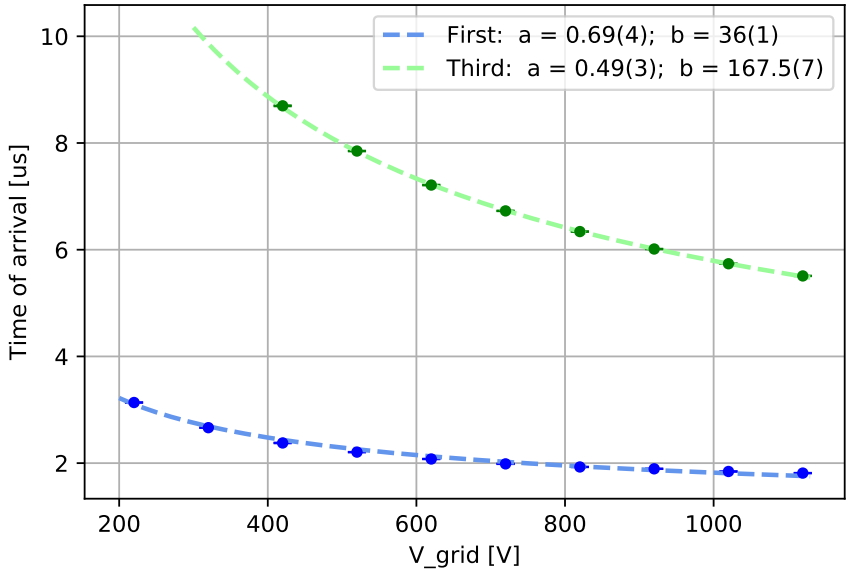

Figure 3.21: ToF analysis of the arrivals pertaining to the first peak (in blue) and to the third peak (in green) of Figure 3.20, with a fit of the ideal model of Eq. 3.3.

In order to characterize the measurements shown in Figure 3.21, we present the key results in the following Table.

Peak	χ^2	$a\,[\mu\text{s}]$	$b\,[\mu\text{s}\,\text{V}^{-1/2}]$	$\frac{m}{q}\,[\frac{u}{e}]$
First	824.4	0.69 ± 0.04	36 ± 1	1.07 ± 0.07
Third	13.5	0.49 ± 0.03	167.5 ± 0.7	23 ± 1

Table 3.3: Table showing the main results of the fits shown in Figure 3.21.

Most of the observations about the results of Figure 3.21 are actually repetitions of things we have already said. Once again, the offsets for the two peaks result compatible to those obtained previously for the same peaks. Moreover, the masses too are compatible with the ones obtained previously and once again point towards the fact that the arrivals pertaining to the first peak consist in H^- ions, while the mass to charge ratio of the particles pertaining to the third peak is between 21 and 25 (95% confidence interval). Also, the increase of the counts pertaining to the third peak suggests that a molecule composed of H atoms is the most likely possibility.

3.2.8 Time of Flight compared to COMSOL simulation

To understand the discrepancy between the ideal model and the data points, we decided to account for the switching time needed by the grid to alternate between positive and negative voltage. In order to do that, we probed with an oscilloscope the voltage on the grid and recorded the shape of the signal. In R. Mosala Nejad Master thesis, one can find the description of a COMSOL simulation of the trajectories of ions of different mass accelerated by the real pos-neg grid pulse. Here, we are just going to take the results of the simulation done by him and confront them with data points from previous measurements. The simulation model that we started with is the following:

$$ToF = a\, V_{\text{neg}}^{b} + c \tag{3.13}$$

The parameters a, b and c are functions of the mass m of the particle:

$$a = \alpha_1\, m^{\alpha_2} + \alpha_3; \qquad b = \beta_1\, m^{\beta_2} + \beta_3; \qquad c = \gamma_1\, m^{\gamma_2} + \gamma_3 \tag{3.14}$$

We note that in the simulation model of Eq. 3.13 there is a mass dependence of the offset c and of the exponent b of V_{neg}, which is not always equal to -0.5. In Figure 3.22 and 3.23 we confront the ToF data of the measurement of Section 3.2.4 with the simulation model of Eq. 3.13.

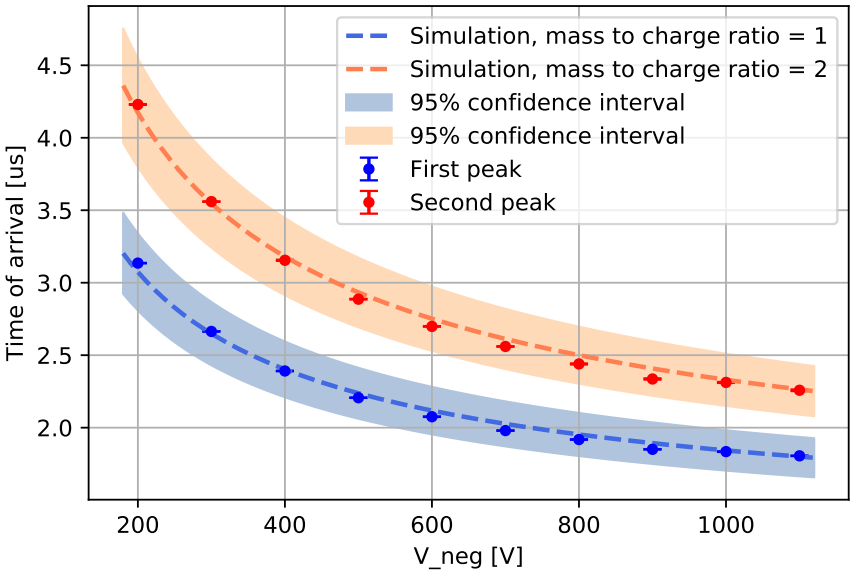

Figure 3.22: ToF data for the first (in blue) and second (in red) peak of the measurement described in Section 3.2.4 with the simulation model for mass-to-charge ratio = 1 (dotted blue line) and for mass-to-charge ratio = 2 (dotted red line). Confidence intervals are 95%.

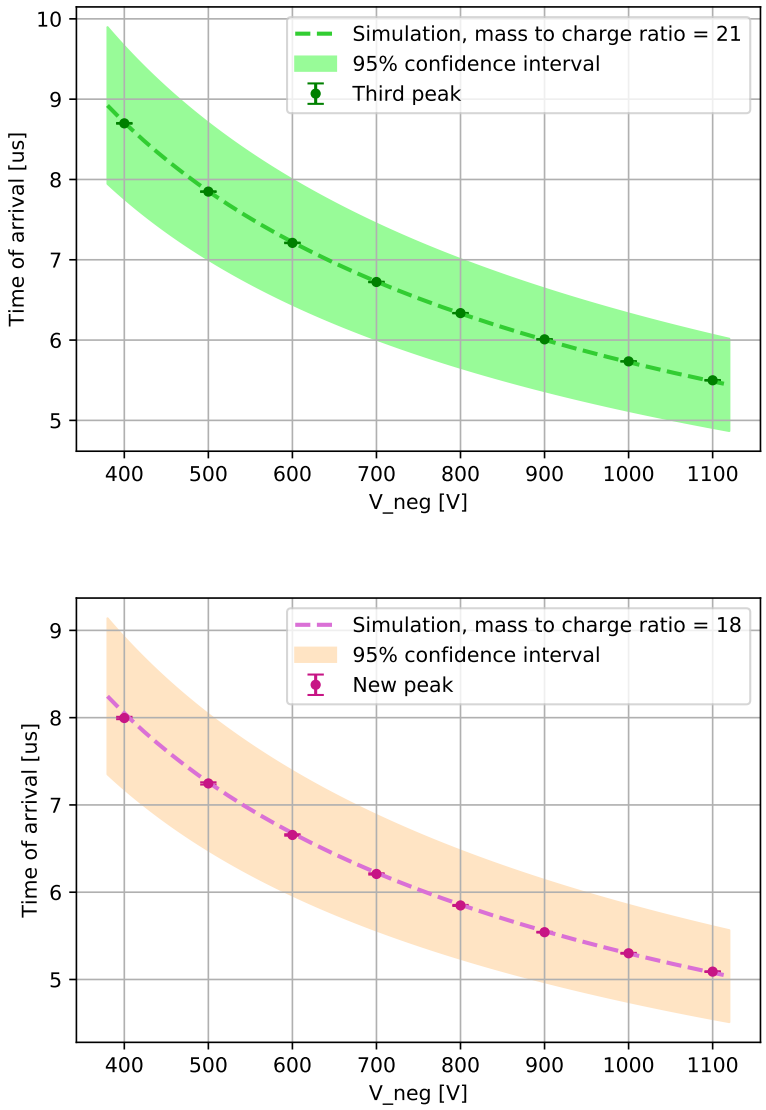

Figure 3.23: ToF data for the third (in green) and new (in magenta) peak of the measurement described in Section 3.2.4 with the simulation model for mass-to-charge ratio = 21 (dotted green line) and for mass-to-charge ratio = 18 (dotted magenta line). Confidence intervals are 95%.

In order to obtain the confidence intervals presented as shaded areas in Figures 3.22 and 3.23, we propagated the uncertainties obtained for the parameters α_i, β_i and γ_i with $i = 1, 2, 3$ by fitting the simulation to the data, to the parameters a, b and c of Eq. 3.13; the shaded areas envelop the curves between $ToF + 2\,\sigma\,ToF$ and $ToF - 2\,\sigma\,ToF$, where $\sigma\,ToF$ is computed for every

V_{neg} by propagating the uncertainties from the parameters a, b and c to ToF. Regarding the offsets, the parameter c of Eq. 3.13 does not account for the offset due to the dead time of the control system, which is not included in the simulation. Thus, for every mass, we added to the simulation offsets c another offset for the dead time of the control system which maximized the agreement between the simulation and the data points. Overall, by averaging over the values of this control system offset for every mass, we get an offset due to the dead time of the control system equal to $0.34 \pm 0.03\,\mu$s.
Regarding the mass-to-charge ratios, the simulation confirms that we have a maximum compatibility between the data points and the output of the model for the first peak having a mass-to-charge ratio of 1, the second peak having a mass-to-charge ratio of 2, the third peak having a mass-to-charge ratio of 21 and the new peak having a mass-to-charge ratio of 18. For the first peak, this confirms our hypothesis of detecting H^- ions, for the second peak D^- is very likely the detected ion. The mass-to-charge ratio of the new peak being equal to 18, together with the fact that this peak was suppressed in the measurement conducted in Section 3.2.7 where the chamber was filled with H_2, suggest that the particle is most likely the anion DO^-. Regarding the third peak, it is still not clear which anion with mass-to-charge ratio of 21 we are detecting, but the considerations made in Section 3.2.7, with the chamber filled up with H_2 molecules, point towards the fact that the ion in question is probably composed also by H atoms. The hypothesis that this detections correspond to light cations that only get accelerated by the positive pulse and for which then the dynamics we are simulating does not apply seems unlikely due to the square root dependence on V_{grid} that we were able to confirm.

3.2.9 Effect of the grid voltage on the number of D^- counts

As a follow up to the measurement shown in Figure 3.7, we can ask what is the dependence on the grid voltage of the total number of counts pertaining to the second peak.
Also, we looked at the spread of the arrivals pertaining to the second peak as a function of the grid voltage V_{grid} by considering the value of the w parameter of the Doniach-Sunjic function of Eq. 3.8 that we fit to the peak. The spread of the arrivals can in principle be an important parameter for the trapping of the D^- ions as some trapping schemes consist in slowing down the incoming ions by the average energy of the beam [17]; a larger spread of the peak of the arrivals corresponds to a wider energy distribution for the arriving particles and thus to larger residual velocities for the slowed down particles once the average energy of the beam has been removed. Overall, it may even be found out while attempting to trap that it is more convenient to have less ions but with a tighter energy distribution; for this reason we measured the values of the spread of the arrivals as a function of V_{grid}.

In order to check the repeatability of the findings, we opted to perform two runs of the experiment. In Figure 3.24 we present the results of the measurement we described.

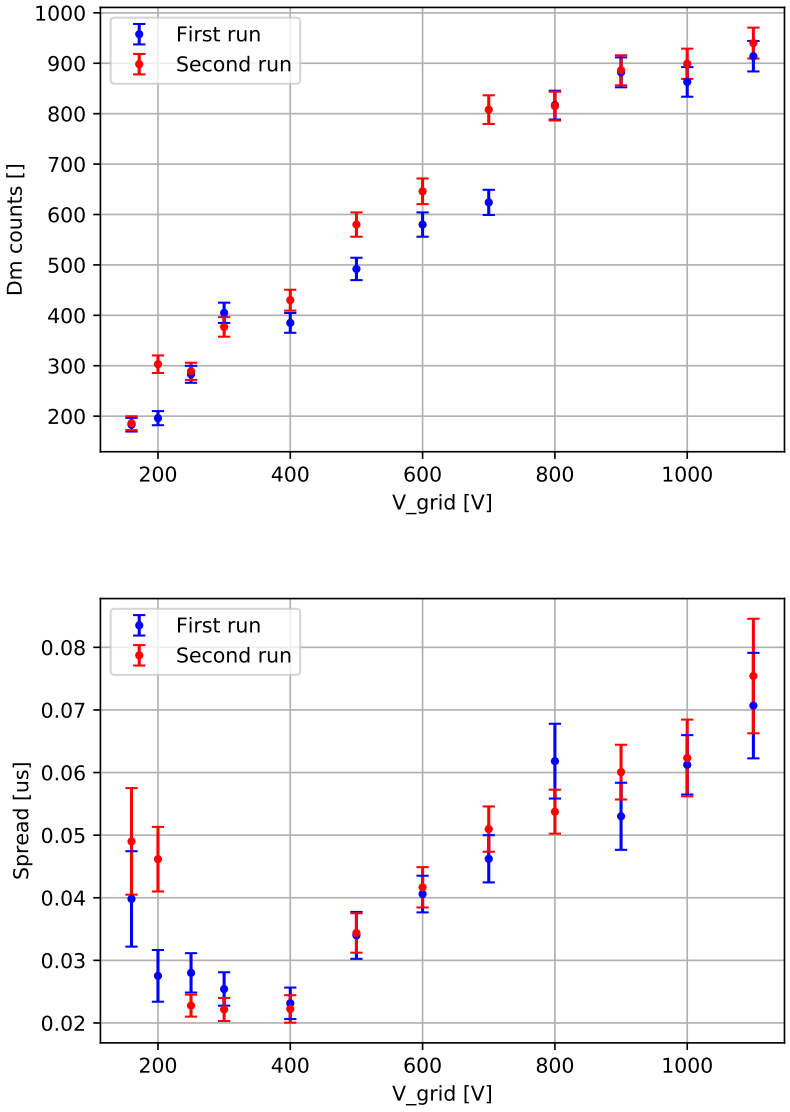

Figure 3.24: The total number of count and the spread of the arrivals pertaining to the second peak as a function of the voltage on the grid V_{grid}, measured in the UHV chamber. In blue we have the points collected in the first run, in red the points for a second run that started just after the first one to test the repeatability of the measurement.

When looking at the total number of counts as a function of V_{grid}, we observe the same trend of Figure 3.7, i.e. they increase for large values of V_{grid} for

both runs, even for the largest values tested. Regarding the spread, from 400 V to 1100 V we observe an increase of a factor of about 3, which may be indicative of a linear dependence of the spread on V_{grid}, at least for the voltage regimes we considered. Again, both runs seem to agree.

Chapter 4

Conclusions and outlook

In the past few months the assembly of a UHV chamber, the implementation of a more efficient control system and the introductions of new elements in the D^- preparation chamber have been carried out by R. Mosala Nejad and myself. We tested the production rate of D^- ions under different experimental conditions both in order to increase the number of ions produced and to improve the quality of the signal. On this note, some of the convictions we had about the production mechanism of the D^- ions were shaken up. Both the acquisition and the analysis of the data from the measurements have become easier, faster and more automatized, thanks to a new implementation of the control system but also to a series of scripts written during the project.
In the near future, it will be important to focus on increasing the total number of D^- ions counts produced in the chamber in order to increase the chances of trapping by for example using the scheme in [17]. The most promising way is probably going to be, in the short run, an optimization of the lens voltage analogous to the one carried out in Section 3.1.4. Other simulations predict an enhancement of the production rate with a two lens configuration for the lens and this should be tested. Measurements such as the one carried out in Section 3.2.6 look promising in order to understand whether with factors such as pressure, temperature and egun voltage we can change the equilibrium between the ions produced and the molecules absorbed into the grid to increase the number of counts.
On the medium to long run, a redesign of the production chamber may be taken into consideration in order to take advantage of surface production processes; for example, building the production chamber around the idea of sputtering may be extremely advantageous. Furthermore, finishing the trap and introducing it inside the UHV chamber will likely take time. Also, cotrapping the D^- and the $^9Be^+$ ions is going to be challenging.
Overall, the project has been moving forward and now consists in a solid platform for new exciting experiments to be undertaken in the future.

Bibliography

[1] *Operating Instructions NEXTORR D 100-5 Pump*. saes group.

[2] TICKOPUR RW77 Special-Cleaner for the ultrasonic bath. *DR H STAMM*.

[3] TICKOPUR TR3 Special-Cleaner for the ultrasonic bath. *DR H STAMM*.

[4] *Vacuum Gauge Controller MGC-3200 User Manual*. Kurt J.Lesker.

[5] J. Kim C. Monroe. Scaling the Ion Trap Quantum Processor. *Science* ***339***, 2013.

[6] P. Chiggiato. Vacuum Technology for Ion Sources. *CERN*, 2012.

[7] D.J. Wineland D. Kielpinski, C. Monroe. Architecture for a large-scale ion-trap quantum computer. *Nature* ***417****, 709–711*, 2002.

[8] J. R. Hiskes. Formation of hydrogen negative ions by surface and volume processes with application to negative ion sources. *Journal de Physique Colloques, 40, C7*, 1979.

[9] S. Koch. *Production and Control of Deuterium Anions and Outlook to Quantum Logic Spectroscopy-based Tests of CPT Violation*. Trapped Ion Quantum Informatio Group, ETHZ, 2021.

[10] H. Liebl. *Applied Charged Particle Optics*. Springer-Verlag Berlin Heidelberg, 2008.

[11] Edmund G. Myers. *CPT* tests with the antihydrogen molecular ion. *Phys. Rev. A*, 98:010101, Jul 2018.

[12] V. Negnevitsky. Feedback-stabilised quantum states in a mixed-species ion system. *PhD Thesis*, 2018.

[13] National Institute of Standards and Technology. *NIST chemistry webbook*. Washington, D.C: National Institute of Standards and Technology, 1997.

[14] M. Sunjic S. Doniach. Many-electron singularity in X-ray photoemission and X-ray line spectra from metals. *J. Phys. C: Solid State Phys.* ***3*** *285*, 1970.

[15] L. Schulz. Sputter-Ion Pumps. *Scanticon Conference Centre, Snekersten, Denmark*, 1999.

[16] E. Krishnakumar *et al.* Dissociative Electron Attachment Cross Section for H_2 and D_2. *Physical Review Letters* ***106****, 243201*, 2011.

[17] G. Cerchiari *et al.* Capture of an external anion beam into a linear Paul trap. *J. Phys. B: At. Mol. Opt. Phys.* ***52*** *155003*, 2019.

[18] K. Oura *et al. Surface Science An Introduction*. Springer, 2003.

[19] G. Tomassi. *Concept analysis and fabrication of an ion trap to couple negative and positive ions*. Trapped Ion Quantum Informatio Group, ETHZ, 2021.

[20] W. Umrath. *Fundamentals of Vacuum Technology*. Oerlikon leybold vacuum, 2007.

[21] G. Vandoni. The basis of Vacuum. *CERN*, Fall 2012.

Eidgenössische Technische Hochschule Zürich
Swiss Federal Institute of Technology Zurich

Declaration of originality

The signed declaration of originality is a component of every semester paper, Bachelor's thesis, Master's thesis and any other degree paper undertaken during the course of studies, including the respective electronic versions.

Lecturers may also require a declaration of originality for other written papers compiled for their courses.

I hereby confirm that I am the sole author of the written work here enclosed and that I have compiled it in my own words. Parts excepted are corrections of form and content by the supervisor.

Title of work (in block letters):

Authored by (in block letters):
For papers written by groups the names of all authors are required.

Name(s):	**First name(s):**

With my signature I confirm that

- I have committed none of the forms of plagiarism described in the 'Citation etiquette' information sheet.
- I have documented all methods, data and processes truthfully.
- I have not manipulated any data.
- I have mentioned all persons who were significant facilitators of the work.

I am aware that the work may be screened electronically for plagiarism.

Place, date	**Signature(s)**

For papers written by groups the names of all authors are required. Their signatures collectively guarantee the entire content of the written paper.